NASA/CR—2004-213199/VOL4

Numerical, Analytical, Experimental Study of Fluid Dynamic Forces in Seals

Volume 4—Description of Incompressible Fluid Seal Codes ICYL and IFACE

Antonio Artiles
Mechanical Technology, Inc., Latham, New York

October 2004

The NASA STI Program Office . . . in Profile

Since its founding, NASA has been dedicated to the advancement of aeronautics and space science. The NASA Scientific and Technical Information (STI) Program Office plays a key part in helping NASA maintain this important role.

The NASA STI Program Office is operated by Langley Research Center, the Lead Center for NASA's scientific and technical information. The NASA STI Program Office provides access to the NASA STI Database, the largest collection of aeronautical and space science STI in the world. The Program Office is also NASA's institutional mechanism for disseminating the results of its research and development activities. These results are published by NASA in the NASA STI Report Series, which includes the following report types:

- TECHNICAL PUBLICATION. Reports of completed research or a major significant phase of research that present the results of NASA programs and include extensive data or theoretical analysis. Includes compilations of significant scientific and technical data and information deemed to be of continuing reference value. NASA's counterpart of peer-reviewed formal professional papers but has less stringent limitations on manuscript length and extent of graphic presentations.

- TECHNICAL MEMORANDUM. Scientific and technical findings that are preliminary or of specialized interest, e.g., quick release reports, working papers, and bibliographies that contain minimal annotation. Does not contain extensive analysis.

- CONTRACTOR REPORT. Scientific and technical findings by NASA-sponsored contractors and grantees.

- CONFERENCE PUBLICATION. Collected papers from scientific and technical conferences, symposia, seminars, or other meetings sponsored or cosponsored by NASA.

- SPECIAL PUBLICATION. Scientific, technical, or historical information from NASA programs, projects, and missions, often concerned with subjects having substantial public interest.

- TECHNICAL TRANSLATION. English-language translations of foreign scientific and technical material pertinent to NASA's mission.

Specialized services that complement the STI Program Office's diverse offerings include creating custom thesauri, building customized databases, organizing and publishing research results . . . even providing videos.

For more information about the NASA STI Program Office, see the following:

- Access the NASA STI Program Home Page at ***http://www.sti.nasa.gov***

- E-mail your question via the Internet to help@sti.nasa.gov

- Fax your question to the NASA Access Help Desk at 301–621–0134

- Telephone the NASA Access Help Desk at 301–621–0390

- Write to:
  NASA Access Help Desk
  NASA Center for AeroSpace Information
  7121 Standard Drive
  Hanover, MD 21076

NASA/CR—2004-213199/VOL4

Numerical, Analytical, Experimental Study of Fluid Dynamic Forces in Seals

Volume 4—Description of Incompressible Fluid Seal Codes ICYL and IFACE

Antonio Artiles
Mechanical Technology, Inc., Latham, New York

Prepared under Contract NAS3–25644

National Aeronautics and
Space Administration

Glenn Research Center

October 2004

Available from

NASA Center for Aerospace Information
7121 Standard Drive
Hanover, MD 21076

National Technical Information Service
5285 Port Royal Road
Springfield, VA 22100

Available electronically at http://gltrs.grc.nasa.gov

FOREWORD

The Computational Fluid Dynamics (CFD) computer codes and Knowledge-Based System (KBS) were generated under NASA contract NAS3-25644 originating from the Office of Advanced Concepts and Technology and administered through NASA-Lewis Research Center. The support of the Program Manager, Anita Liang, and the advice and direction of the Technical Monitor, Robert Hendricks, are gratefully appreciated. Major contributors to code development were:

- Dr. Bharat Aggarwal: KBS and OS/2 PC conversion of labyrinth seal code KTK
- Dr. Antonio Artiles: cylindrical and face seal codes ICYL and IFACE
- Dr. Mahesh Athavale and Dr. Andrzej Przekwas: CFD code SCISEAL
- Mr. Wilbur Shapiro: gas cylindrical and face seal codes GCYLT, GFACE, and seal dynamics code DYSEAL
- Dr. Jed Walowit: spiral groove gas and liquid cylindrical and face seal codes SPIRALG and SPIRALI.

The labyrinth seal code, KTK, was developed by Allison Gas Turbine Division of General Motors Corporation for the Aero Propulsion Laboratory, Air Force Wright Aeronautical Laboratories, Wright-Patterson Air Force Base, Ohio. It is included as part of the CFD industrial codes package by the permission of the Air Force.

TABLE OF CONTENTS

SECTION	PAGE
FOREWORD	iii
LIST OF FIGURES	vii
LIST OF TABLES	ix
NOMENCLATURE	xi
1.0 INTRODUCTION	1
2.0 THEORETICAL DESCRIPTION AND NUMERICAL METHODS	3
2.1 Governing Equations	9
2.2 Solution of Film Pressures	16
2.3 Solution of Flow Velocity	20
2.4 Fluid Film Load, Moment and Torque	23
2.5 Stiffness and Damping Coefficients	28
2.6 Solution of Rotor Position and Pocket Pressures	28
3.0 SAMPLE PROBLEMS FOR CODE ICYL	31
4.0 SAMPLE PROBLEMS FOR CODE IFACE	49
5.0 VERIFICATION	59
5.1 Comparison Against Other MTI Codes	59
5.2 Comparison Against Published Data	59
6.0 REFERENCES	69

LIST OF FIGURES

NUMBER		PAGE
1	Cylindrical Seal Geometry	4
2	Axial Cross Section of Seal with Eccentric Rotor	5
3	Face Seal Geometry	6
4	Rotor with Lateral and Angular Displacements	7
5	Arbitrary Film Thickness Specification	8
6	Friction Factor versus Reynolds Number	11
7	Detail of Friction Factor in Transition Region	12
8	Flow Control Area About Grid Point I,J	17
9	Example of Cell at Corner of Pocket	19
10	Schematic of Rectangular Region Between Grid Lines	21
11	Film Thickness Distribution for Sample EX3	33
12	Pressure Distribution for Sample EX3	34
13	Film Thickness Distribution for Sample F3	36
14	Pressure Distribution for Sample F3	37
15	Film Thickness Distribution for Sample F4	38
16	Pressure Distribution for Sample F4	39
17	Film Thickness Distribution for Sample F9	40
18	Pressure Distribution for Sample F9	41
19	Pressure Distribution for Sample I1	42
20	Film Thickness Distribution for Sample I2	43
21	Pressure Distribution for Sample I2	44
22	Pressure Distribution for Sample I5	45
23	Film Thickness Distribution for Sample I6	46
24	Pressure Distribution for Sample I6	47
25	Critical Mass Versus Housing Roughness	48
26	Film Thickness Distribution for Sample 1	51
27	Pressure Distribution for Sample 1	51
28	Film Thickness Distribution for Sample 2A	52
29	Pressure Distribution for Sample 2A	52
30	Film Thickness Distribution for Sample 3B	54
31	Pressure Distribution for Sample 3B	54
32	Film Thickness Distribution for Sample 13	55
33	Pressure Distribution for Sample 13	55
34	Film Thickness Distribution for Sample 17	57
35	Pressure Distribution for Sample 17	57
36	Film Thickness Distribution for Sample 15B	58
37	Pressure Distribution for Sample 15B	58
38	Comparison to San Andrés Five-Pad Bearing at Concentric Position	61
39	Comparison to San Andrés Five-Pad Bearing With 40% Eccentricity Between Pockets	62

LIST OF FIGURES (Continued)

NUMBER PAGE

40 Comparison to San Andrés Five-Pad Bearing
With 40% Eccentricity Over Pocket 63
41 Comparison of Direct Stiffness Coefficient 65
42 Comparison of Cross Stiffness Coefficients 65
43 Comparison of Direct Damping Coefficients 66
44 Comparison of Cross Damping Coefficients 66
45 Critical mass versus Eccentricity Ratio 67

LIST OF TABLES

NUMBER		PAGE
1	Summary of Sample Cases for Code ICYL	32
2	Summary of Sample Cases	50
3	Effect of Roughness on Torque and Direct Stiffnesses	56
4	Comparison Against GBEAR	60

NOMENCLATURE

A, B	Misalignment of rotor about the x and y axes, respectively [radians]
$b_{ij} = B_{ij}\,(C^3/12\mu R^4)$	Dimensionless damping coefficient matrix, where i, j = x, y, z, α, β
C	Nominal clearance [L]
e	Rotor eccentricity at $z = 0$ [L]
e_b, e_j	Roughness of the housing and journal surfaces [L]
e_x, e_y, e_z	Components of rotor eccentricity [L]
$\hat{\mathbf{e}}_\zeta$, $\hat{\mathbf{e}}_\theta$	Unit vectors in the meridional and circumferential directions
F_x, F_y, F_z	Components of fluid film force [F]
$f = F/(P_oR^2)$	Dimensionless fluid film force
H	Local film thickness [L]
H_o	Local film thickness for the concentric aligned rotor (i.e., $e_x = e_y = e_z = A = B = 0$) [L]
$h = H/C$	Dimensionless local film thickness
K_e	Dimensionless coefficient of pressure drop at inlet to film
K_{ij}, B_{ij}	Stiffness and damping coefficient matrices, where i, j= x, y, z, α, β
$k_{ij} = K_{ij}\,(C/P_oR^2)$	Dimensionless stiffness coefficient matrix, where i, j, = x, y, α, β
L	Meridional extent of seal surface (seal length for a cylindrical seal and radial extent for a face seal) [L]
M_x, M_y	Components of fluid film force about x and y axes [F-L]
$m = M/(P_oR^3)$	Dimensionless fluid film moment
$\hat{\mathbf{n}}$	Unit vector normal to fluid film boundary
P	Local pressure [F/L^2]
$p = P/P_o$	Dimensionless local pressure
P_l, P_r	Left and right boundary pressures for a cylindrical seal (boundary pressures at inner and outer radii for a face seal). [F/L^2]
P_p, P_s	Pocket and supply pressures [F/L^2]
P_o	Reference pressure, used for scaling the pressure field (set internally by program to maximum of P_s, P_l or P_r) [F/L^2]
Q_r	Flow from pocket or recess [L^3/T]
$q_r = Q_r\,(12\mu/P_oC^3)$	Dimensionless flow from pocket or recess
R	Seal radius for a cylindrical seal, outer radius for a face seal [L]

$Re^* = \rho h^3 \nabla p/\mu^2$	Local Reynolds number based on pressure-driven flow
$Re_o^* = \rho C^3 P_o/(R\mu^2)$	Reference Reynolds number based on pressure-driven flow
t	Time [T]
$u = U\,(12\mu R/C^2 P_o)$	Dimensionless circumferential component of fluid velocity
$v = V\,(12\mu R/C^2 P_o)$	Dimensionless meridional component of fluid velocity
U, V	Circumferential and meridional fluid velocity components, averaged across the film [L/T]
U_b, U_j	Linear velocity of housing and journal surfaces (equal to $R\omega_b$, $R\omega_j$, respectively) [L/T]
X,Y,Z	Cartesian coordinates [L]
ζ	Dimensionless meridional coordinate (Z/R for a cylindrical seal, r/R for a face seal)
α	Misalignment ratio about the x-axis
β	Misalignment ratio about the y-axis
ε_x, ε_y, ε_z	Components of rotor eccentricity ratio ($\varepsilon = e/C$)
$\varepsilon = e/C$	Rotor eccentricity ratio
θ	Circumferential coordinate [radians]
$\Lambda_b = 6\mu U_b R/(C^2 P_o)$	Dimensionless velocity of housing surface
$\Lambda_j = 6\mu U_j R/(C^2 P_o)$	Dimensionless velocity or rotor surface
$\Lambda_r = \rho C^6 P_o/(288\, A_o^2 C_d^2 \mu^2)$	Coefficient of orifice restriction
$\Lambda_e = K_e\,(Re_o^* C/288\, R)$	Coefficient of pressure drop at inlet to film
μ	Fluid dynamic viscosity [F-S/L^2]
ρ	Fluid density [F-T^{2}L^{-4}]
ω_b, ω_j	Angular velocity of housing and journal surfaces [rad/T]
$\tau = t\,(C^2 P_o/12\mu R^2)$	Dimensionless time

1.0 INTRODUCTION

NASA's advanced engine programs are aimed at progressively higher efficiencies, greater reliability, and longer life. Recent studies have indicated that significant engine performance advantages can be achieved by employing advanced seals [1]*, and dramatic life extensions can also be achieved. Advanced seals are not only required to control leakage, but are necessary to control lubricant and coolant flow, prevent entrance of contamination, inhibit the mixture of incompatible fluids, and assist in the control of rotor response.

Recognizing the importance and need of advanced seals, NASA, in 1990, embarked on a five-year program (Contract NAS3-25644) to provide the U.S. aerospace industry with computer codes that would facilitate configuration selection and the design and application of advanced seals.

The program included four principal activities:

1. Development of a scientific code called SCISEAL, which is a Computational Fluid Dynamics (CFD) code capable of producing full three-dimensional flow field information for a variety of cylindrical configurations. The code is used to enhance understanding of flow phenomena and mechanisms, to predict performance of complex situations, and to furnish accuracy standards for the industrial codes. The SCISEAL code also has the unique capability to produce stiffness and damping coefficients that are necessary for rotordynamic computations.
2. Generation of industrial codes for expeditious analysis, design, and optimization of turbomachinery seals. The industrial codes consist of a series of separate stand-alone codes that were integrated by a Knowledge-Based System (KBS).
3. Production of a KBS that couples the industrial codes with a user friendly Graphical User Interface (GUI) that can in the future be integrated with an expert system to assist in seal selection and data interpretation and provide design guidance.
4. Technology transfer via four multiday workshops at NASA facilities where the results of the program were presented and information exchanged among suppliers and users of advanced seals. A Peer Panel also met at the workshops to provide guidance and suggestions to the program.

This final report has been divided into separate volumes, as follows:

Volume 1: Executive Summary and Description of Knowledge-Based System
Volume 2: Description of Gas Seal Codes GCYLT and GFACE
Volume 3: Description of Spiral-Groove Codes SPIRALG and SPIRALI
Volume 4: Description of Incompressible Seal Codes ICYL and IFACE
Volume 5: Description of Seal Dynamics Code DYSEAL and Labyrinth Seal Code KTK
Volume 6: Description of Scientific CFD Code SCISEAL.

This volume describes the codes ICYL (incompressible, cylindrical) and IFACE (incompressible, face) that determine performance of a variety of incompressible fluid-film

*Numbers in brackets designate references presented in Section 6.0.

seal configurations. Both were written in FORTRAN for a PC environment using OS/2 as an operating system. References 2 and 3 provide the details of code implementation.

The computer code ICYL was developed [1] to evaluate the performance of cylindrical seals operating with incompressible fluids. The computer code IFACE was subsequently developed to also handle face seals. The pressures generated in plain cylindrical seals with incompressible fluids typically result in forces which are normal to the displacement and therefore tend to destabilize the rotating shaft. Surface roughness, geometry alterations, and external pressurization are ways in which the direct stiffness and damping coefficients can be improved and the cross-coupled stiffness decreased in order to improve stability.

The pressure and velocity distributions within the seal clearance are first evaluated from the governing equations. From these, design quantities such as seal leakage flows, power loss and resulting forces and moments are calculated. Minimum film thicknesses and maximum pressures as well as critical rotor-dynamics coefficients such as stiffness, damping and critical mass are evaluated.

Program capabilities:

1. 2-D incompressible isoviscous flow in cylindrical and face geometry.
2. Rotation of both rotor and housing.
3. Roughness of both rotor and housing.
4. Arbitrary film thickness distribution, including features such as steps, pockets, tapers and preloaded arcs
5. Rotor position described by four degrees of freedom (translational and rotational)
6. Up to 32 dynamic coefficients as well as the critical mass may be calculated for use in rotor-dynamic design, including system response and stability calculations.
7. Steady external forces and/or moments may be prescribed to find the position of the rotor relative to the housing.
8. Pocket pressures or orifice size are prescribed.
9. Laminar or turbulent flow.
10. Cavitation.
11. Inertia pressure drop at inlets to fluid film (from ends of seal and from pressurized pockets).

Assumptions:

1. The film thickness is assumed to be small compared with seal lengths and diameters but large compared with surface roughness.
2. Pockets supplied from an external pressure source through an orifice restriction are assumed to be sufficiently deep that the pressure is constant within them.
3. Wall roughness is assumed to be isotropic and represented by an "equivalent sand roughness" height.
4. Fluid inertia effects in the film are negligible.

This report describes the fundamental theory, sample problems and code validation.

2.0 THEORETICAL DESCRIPTION AND NUMERICAL METHODS

Figures 1 and 2 illustrate the geometry of a cylindrical seals as well as the coordinate system used to describe it. Figure 1 shows the seal housing of length L separated from the rotor by the film thickness C. The coordinate system is placed at the mid-length of the seal with the circumferential coordinate θ measured from the x-axis. Figure 2 shows an axial cross-section of the film thickness with an eccentric rotor. Figure 3 similarly illustrates the geometry and coordinate system used to describe a face seal, from side and end views. The top part illustrates the seal ring rotating with a stationary mating ring, while the bottom illustrates the reversed situation. Figure 4 illustrates the lateral and angular displacements of the rotor as well as the direction of the fluid film forces and moments.

For the cylindrical geometry, the film thickness and time derivative are written:

$$H = H_o - (e_x + ZB)\cos\theta - (e_y - ZA)\sin\theta$$

$$\frac{\partial H}{\partial t} = -\left(\frac{\partial e_x}{\partial t} + Z\frac{\partial B}{\partial t}\right)\cos\theta - \left(\frac{\partial e_y}{\partial t} - Z\frac{\partial A}{\partial t}\right)\sin\theta \tag{1}$$

where H_o, an arbitrary function of film coordinates, represents the film thickness distribution for a rotor that is aligned and centered with the housing. A and B represent the angles of rotor rotation about the x and y axes, respectively, while e_x and e_y represent the components of rotor eccentricity at the seal mid-length. The former are referred to as the angular displacements and the latter as the lateral displacements.

For the face geometry,

$$H = H_o + e_z - Br\cos\theta + Ar\sin\theta$$

$$\frac{\partial H}{\partial t} = \frac{\partial e_z}{\partial t} - \frac{\partial B}{\partial t}r\cos\theta + \frac{\partial A}{\partial t}r\sin\theta \tag{2}$$

where r is the local radius and e_z represents an axial eccentricity of the rotor away from the housing.

One innovative feature of the code is the ability to specify recessed regions in the field with bi-directional tapers, as shown on Figure 5, by specifying the depths at the corner points of the region and using linear variations between the corner points.

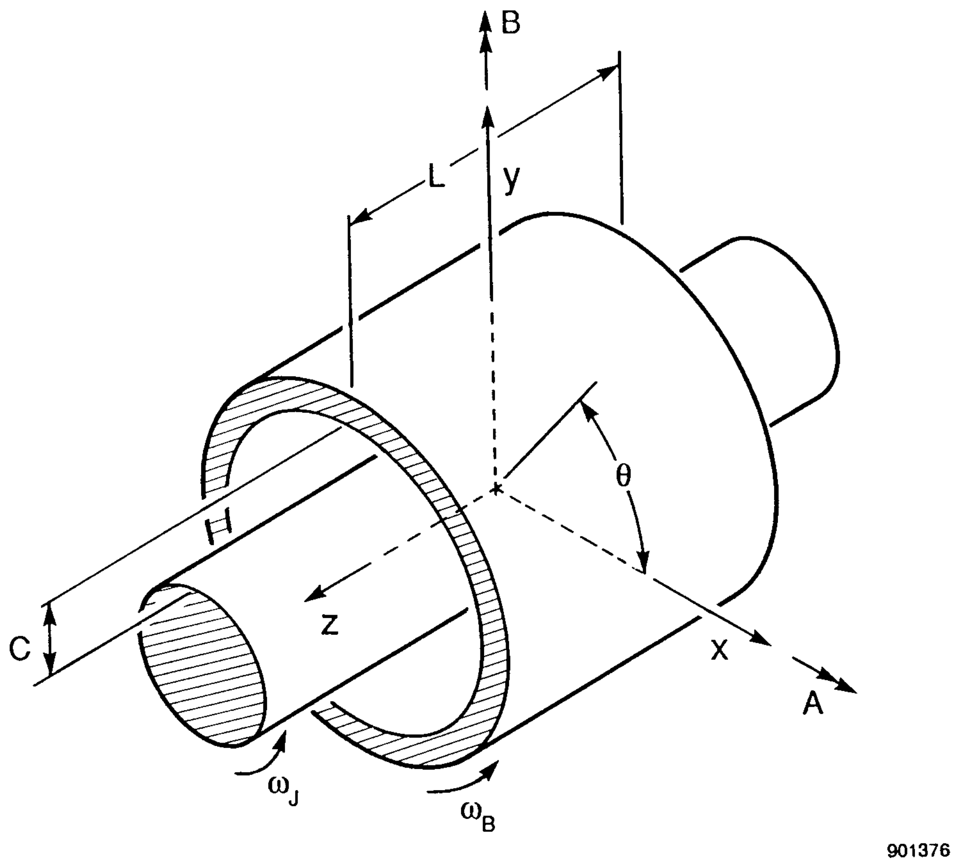

Figure 1. Cylindrical Seal Geometry

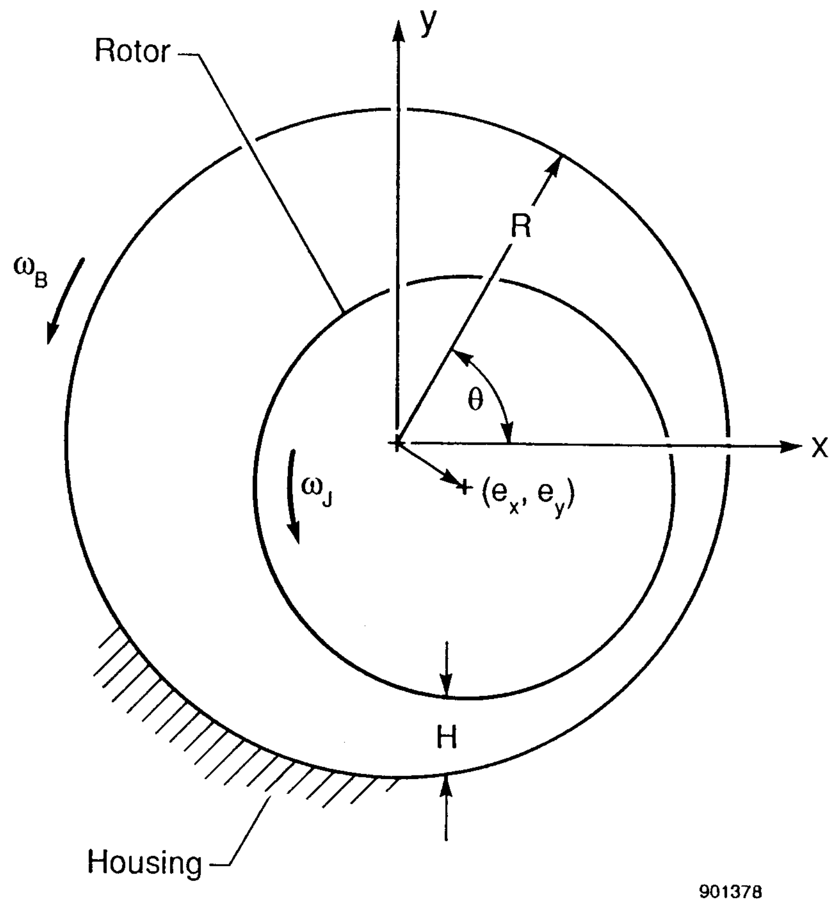

Figure 2. Axial Cross Section of Seal with Eccentric Rotor

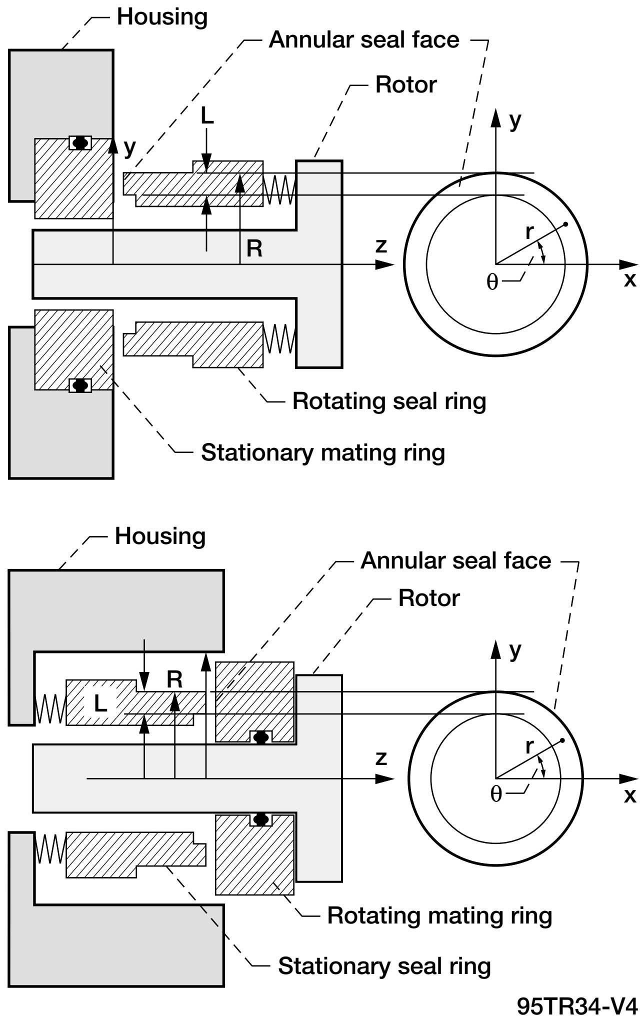

Figure 3. Face seal geometry.

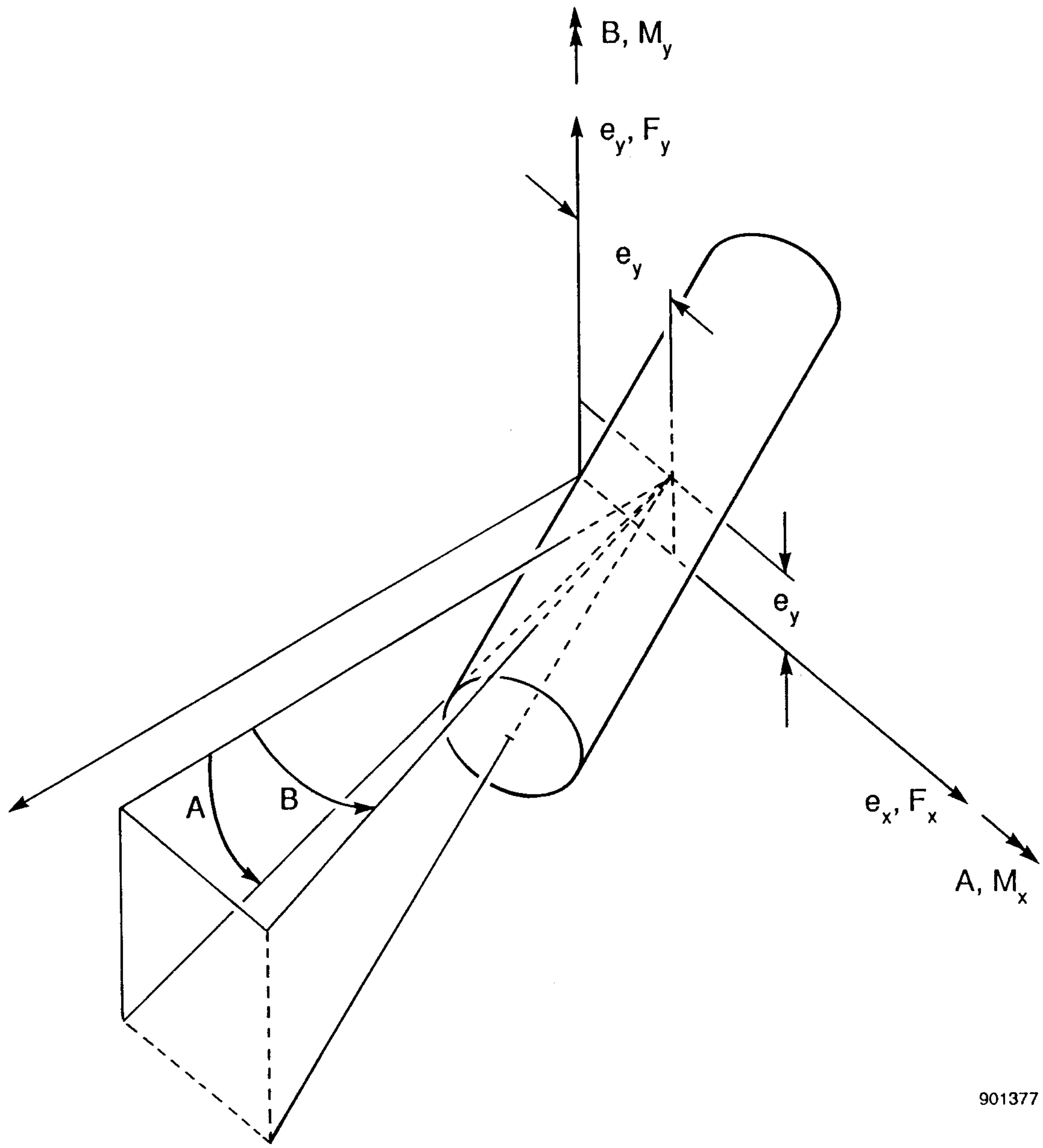

Figure 4. Rotor with Lateral and Angular Displacements

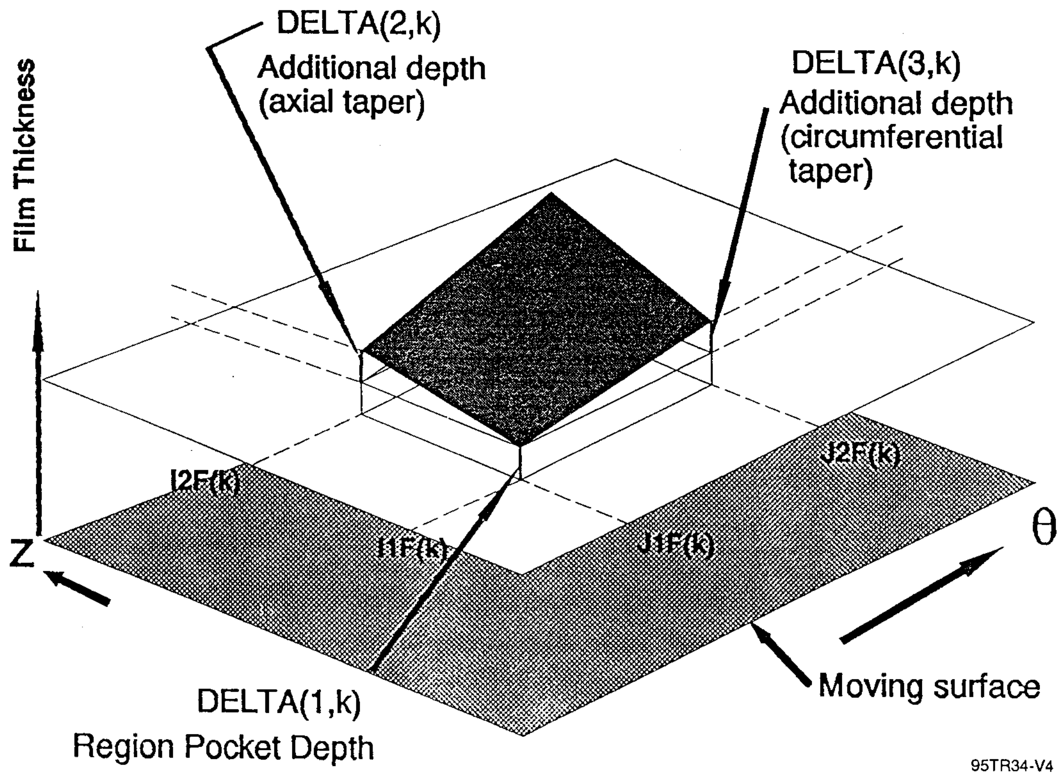

Figure 5. Arbitrary Film Thickness Specification

2.1 Governing Equations

The equations governing the flow of incompressible fluids in thin films are obtained [4,5,6] by integrating the Navier-Stokes momentum and continuity equations across the film*:

$$
\begin{aligned}
\frac{(f_j Re_j + f_b Re_b)}{2} U &= -\frac{H^2}{\mu r}\frac{\partial P}{\partial \theta} + \frac{(Re_j f_j U_j + Re_b f_b U_b)}{2} \\
\frac{(f_j Re_j + f_b Re_b)}{2} V &= -\frac{H^2}{\mu R}\frac{\partial P}{\partial \zeta}
\end{aligned}
\qquad (3)
$$

$$
\frac{1}{r}\frac{\partial}{\partial \theta}(UH) + \frac{1}{R}\frac{\partial}{\partial \zeta}(VH) + \frac{\partial H}{\partial t} = 0 \qquad (4)
$$

where f_j and f_b are the friction factors relative to the housing and journal surfaces, respectively, and are functions of the Reynolds numbers relative to these surfaces as well as their roughness. They are given by:

$$
Re_i = \frac{\rho H}{\mu}\sqrt{(U-U_i)^2 + V^2} \qquad (5)
$$

where i=j,b, and

$$
f_i = \begin{cases}
\dfrac{12}{Re_i}\,, \quad Re_i \le 1000 \qquad (laminar) \\
\dfrac{12}{Re_i}(1 - 3\xi^2 + 2\xi^3) + f_i^*(3\xi^2 - 2\xi^3), \quad 1000 < Re_i < 3000 \\
f_i^*\,, \quad Re_i \ge 3000 \qquad (turbulent)
\end{cases}
\qquad (6)
$$

$$
\begin{aligned}
\xi &\equiv \frac{Re_i - 1000}{2000} \\
f_i^* &= 0.001375\left[1 + \left(\frac{10^4 e_i}{H} + \frac{10^6}{2 Re_i}\right)^{\frac{1}{3}}\right]
\end{aligned}
\qquad (7)
$$

*_Film_ and _film thickness_ are used to mean the gap of lubricant separating the rotor and housing.

The friction factor for turbulent flow through pipes, f^*, in equation (7) uses the curve-fit obtained by Nelson [7] to Moody's data. The transition from laminar to turbulent flow is obtained using a cubic polynomial which matches values and slopes at both ends, as reflected by equation (6). Figure 6 is a plot of the friction factor versus Reynolds number and surface roughness, while Figure 7 is an enlargement showing the detail of the transition region.

Under laminar flow the friction factors are equal to 12/Re and the momentum equations can be solved explicitly for the velocities in terms of the pressure gradients:

$$U = -\frac{12H^2}{\mu R}\frac{\partial P}{\partial \theta} + R\frac{\omega_j + \omega_b}{2}$$
$$V = -\frac{12H^2}{\mu R}\frac{\partial P}{\partial \zeta} \tag{8}$$

There is no effect of roughness if the flow is laminar.

Lubrication Background

In the classical theory of lubrication, when the housing is stationary and the rotor wall velocity is $U_j=\omega r$, the fluid velocity components are expressed explicitly in terms of the pressure gradients:

$$U = -\frac{H^2 G_x}{12\mu r}\frac{\partial p}{\partial \theta} + \frac{\omega r}{2}, \quad V = -\frac{H^2 G_z}{12\mu R}\frac{\partial p}{\partial \zeta} \tag{9}$$

where G_x and G_z are turbulence coefficients [8] which become unity in the laminar regime. Substituting these velocity components into the continuity equation, results in the classical Reynold's equation:

$$\frac{1}{r^2}\frac{\partial}{\partial \theta}\left(H^3 G_x \frac{\partial P}{\partial \theta}\right) + \frac{1}{R^2}\frac{\partial}{\partial \zeta}\left(H^3 G_z \frac{\partial P}{\partial \zeta}\right) = 6\mu\omega\frac{\partial H}{\partial \theta} + 12\mu\frac{\partial H}{\partial t} \tag{10}$$

Boundary Conditions

Boundary conditions on the film pressure distribution consist of prescribing either the pressure at the boundaries of the film, the flow normal to these boundaries, or a relation between these two quantities.

At the circumferential ends of the seal surface model, either the pressures are prescribed:

$$P = 0 \text{ at } \theta = \theta_s \text{ and } P = 0 \text{ at } \theta = \theta_e,$$

or periodic boundary conditions exists:

$$P(\theta = \theta_s) = P(\theta = \theta_e) \text{ and } U(\theta = \theta_s) = U(\theta = \theta_e)$$

Periodic boundary conditions are used, for example, for a 360° seal, where $\theta_e=\theta_s+2\pi$.

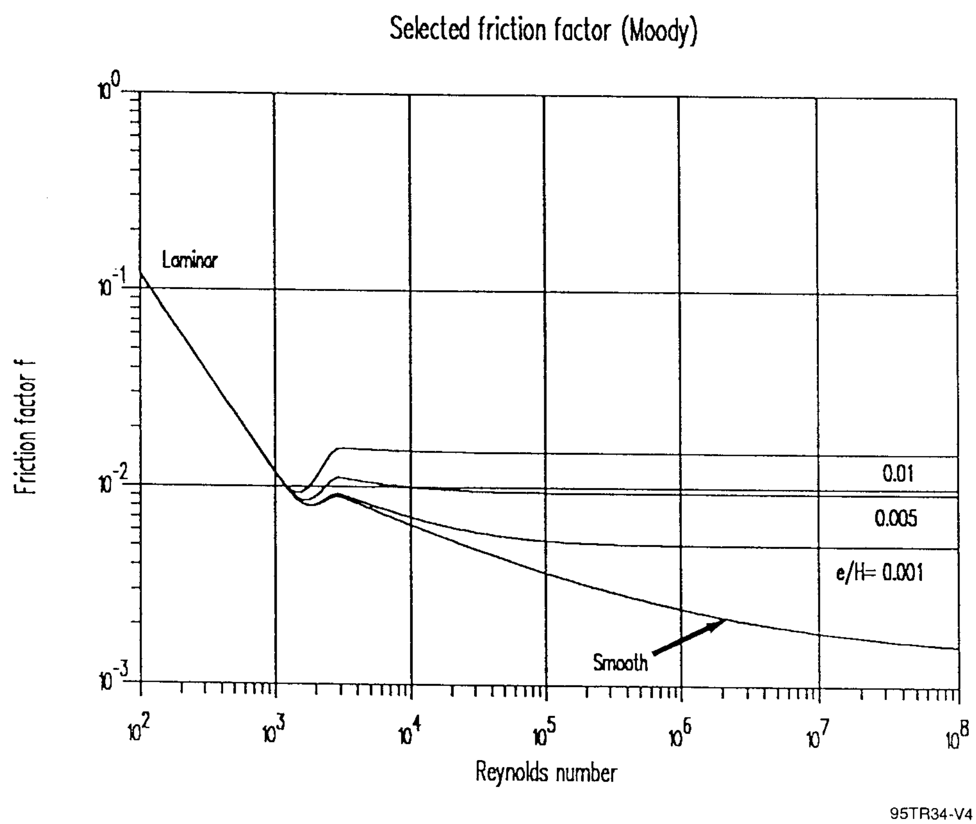

Figure 6. Friction Factor versus Reynolds Number

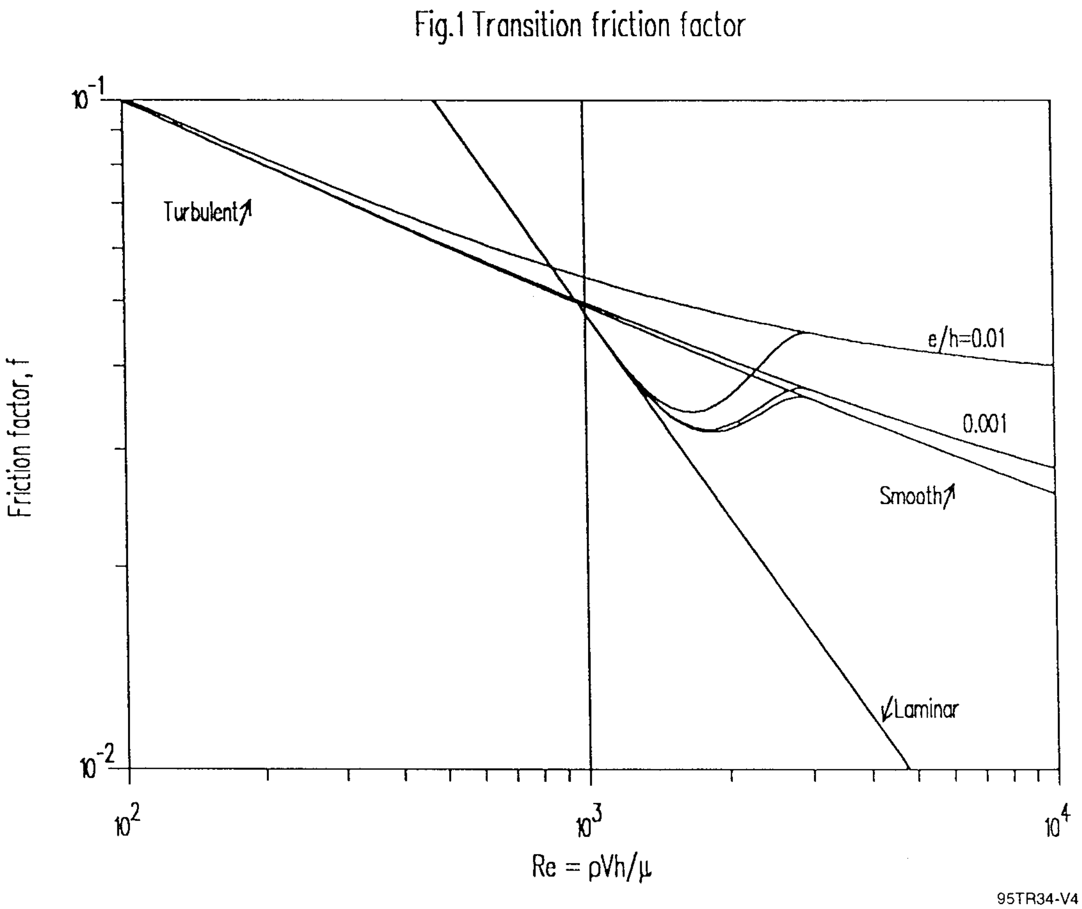

Figure 7. Detail of Friction Factor in Transition Region

For a cylindrical seal the pressure/flow relationship is prescribed by:

$$P = P_l - K_e \tfrac{1}{2}\rho V_n^2 \quad \text{and} \quad P = P_r - K_e \tfrac{1}{2}\rho V_n^2$$

at the left and right ends of the seal surface model, respectively. When a symmetry boundary is present at the seal mid-length, only the left half ($-\frac{1}{2}L \le z \le 0$) of the seal is modeled and the right end relationship is replaced by a zero axial velocity, $V(0,\theta)=0$. For a face seal, the same relationships are used at the inner and outer radii, although no symmetry boundary is possible.

$$P = P_l - K_e \tfrac{1}{2}\rho V_n^2 \quad \text{and} \quad P = P_r - K_e \tfrac{1}{2}\rho V_n^2$$

At pocket boundaries, the relationship of film pressure to flow is written:

$$P = P_p - K_e \tfrac{1}{2}\rho V_n^2.$$

In all of the above relationships, V_n is the flow velocity at the entrance to the film, normal to the pressurized boundary and given by:

$$V_n = \begin{cases} \vec{V}\cdot\hat{n}, & \vec{V}\cdot\hat{n} > 0 \\ 0, & \vec{V}\cdot\hat{n} \le 0 \end{cases} \tag{11}$$

$$\vec{V} \equiv U\hat{e}_z + V\hat{e}_\theta$$

No pressure drop exists in the case of reverse flow (i.e., flow into the pressurized boundary).

External Pressurization

The pressure drop across the orifice supplying the pocket is given by:

$$P_s - P_p = sgn(Q_r)\,\frac{\rho}{2}\left(\frac{Q_r}{A_o C_d}\right)^2 \tag{12}$$

where A_o is the orifice area, C_d is the discharge coefficient and the flow Q_r is obtained by satisfying continuity over the pocket volume:

$$Q_r = \oint_{S_p} H\,\vec{V}\cdot\hat{n}\,dS + \int_{A_p} \frac{\partial H}{\partial t}\,dA \tag{13}$$

where A_p is the pocket area, S_p is its perimeter. The contribution of $\mathbf{V}\cdot\hat{\mathbf{n}}$ to this last equation may be positive or negative.

Dimensionless Variables

Using the following transformation to dimensionless variables,

$b = B\,(C^3/12\,\mu R^4)$	$\tau = t\,(C^2P_o/12\,\mu R^2)$
$f = F/(P_oR^2)$	$\Lambda_b = 6\,\mu U_bR/(C^2P_o)$
$h = H/C$	$\Lambda_j = 6\,\mu U_jR/(C^2P_o)$
$k = K\,(C/P_oR^2)$	$\varepsilon = e/C$
$m = M/(P_oR^3)$	$\alpha = A\,(R/C)$
$p = P/P_o$	$\beta = B\,(R/C)$
$q_r = Q_r\,(12\,\mu/P_oC^3)$	$Re^* = \rho h^3\nabla p/\,\mu^2$
$u = U\,(12\,\mu R/C^2P_o)$	$Re_o^* = \rho C^3P_o/(R\,\mu^2)$
$v = V\,(12\,\mu R/C^2P_o)$	$\Lambda_r = \rho C^6P_o/(288\,A_o^2C_d^2\,\mu^2)$
$\zeta = Z/R$ for cylindrical geometry	$= (Re_o^*/288)\,(C^3R/A_o^2C_d^2)$
$= r/R$ for face geometry	$\Lambda_e = K_e\,(Re_o^*C/288\,R)$,

the dimensionless film thickness is now written for the cylindrical geometry:

$$h = h_o - (\varepsilon_x + z\beta)\cos\theta - (\varepsilon_y - z\alpha)\sin\theta$$

$$\frac{\partial h}{\partial \tau} = -\left(\frac{\partial \varepsilon_x}{\partial \tau} + z\frac{\partial \beta}{\partial \tau}\right)\cos\theta - \left(\frac{\partial \varepsilon_y}{\partial \tau} - z\frac{\partial \alpha}{\partial \tau}\right)\sin\theta \tag{14}$$

and for the face geometry:

$$h = h_o + \epsilon_z - \beta\zeta\cos\theta + \alpha\zeta\sin\theta$$

$$\frac{\partial h}{\partial \tau} = \frac{\partial \epsilon_z}{\partial \tau} - \frac{\partial \beta}{\partial \tau}\zeta\cos\theta + \frac{\partial \alpha}{\partial \tau}\zeta\sin\theta \tag{15}$$

Equations (3), (4) and (5) become:

$$\frac{(f_jRe_j + f_bRe_b)}{2}u = -12h^2\frac{\partial p}{\partial \theta} + (Re_jf_j\Lambda_j + Re_bf_b\Lambda_b)$$

$$\frac{(f_jRe_j + f_bRe_b)}{2}v = -12h^2\frac{\partial p}{\partial z} \tag{16}$$

$$\frac{\partial}{\partial\theta}(uh) + \frac{\partial}{\partial z}(vh) + \frac{\partial h}{\partial\tau} = 0 \tag{17}$$

$$Re_i = \frac{Re_o^* h}{12}\sqrt{(u-2\Lambda_i)^2 + v^2}, \quad i = j,b \tag{18}$$

Equations (6) and (7) remained unaltered, as they were already dimensionless.

The dimensionless form of the boundary conditions now become, at the circumferential ends, either

$$p(\zeta,\ \theta_s) = 0 \ \text{ and } \ p(\zeta,\ \theta_e) = 0$$

or

$$p(\zeta,\ \theta_s) = p(\zeta,\ \theta_e) \text{ and } u(\zeta,\ \theta_s) = u(\zeta,\ \theta_e)$$

when periodic boundary conditions are present. At the left end, the dimensionless boundary conditions become

$$p(-L/D,\theta) = p_l - \Lambda_e v_n^2$$

and at the right end, either

$$p(L/D,\theta) = p_r - \Lambda_e v_n^2$$

or

$$v(0,\theta) = 0.$$

At pocket boundaries

$$p(z,\theta) = p_p - \Lambda_e v_n^2$$

where:

$$v_n = \begin{cases} \boldsymbol{V}\cdot\hat{\boldsymbol{n}}, & \boldsymbol{V}\cdot\hat{\boldsymbol{n}} > 0 \\ 0, & \boldsymbol{V}\cdot\hat{\boldsymbol{n}} \le 0 \end{cases} \tag{19}$$

$$\boldsymbol{V} \equiv u\hat{\boldsymbol{e}}_z + v\hat{\boldsymbol{e}}_\theta$$

Equations (12) and (13) governing the external pressurization become:

$$p_s - p_p = sgn(q_r)\,\Lambda_r q_r^2 \tag{20}$$

$$q_r = \oint_{S_p} h \; v \cdot \hat{n} \; ds + \int_{A_p} \frac{\partial h}{\partial \tau} \, d\theta \, dz \tag{21}$$

2.2 Solution of Film Pressures

Discretization of the seal surface is done by using a rectangular grid, with **M** lines in the meridional direction and **N** lines in the circumferential direction. The grid lines are separated by variable increments. The pressure distribution is represented by discrete values at the grid points located at the intersections of the grid lines. There must be grid lines coincident with the boundaries of the seal surface and with the pocket boundaries. Using the cell method [9], a control area or cell is centered at each grid point and extending half way to the neighboring grid lines, as shown by the shaded area in Figure 8. The grid points are noted by the solid circles and have grid coordinates i,j. The film thickness is evaluated at the corners of the cell (denoted by the shaded circles marked h_1, h_2, h_3, and h_4) located at the geometric centers of the rectangles formed by the grid lines. This staggered configuration allows a discontinuous film thickness to be treated, as occurs, for example in a seal with a Rayleigh-step. Circumferential and meridional components of velocity are also associated with each of the four cell corners.

Using the divergence theorem, the continuity equation may be integrated over the cell to give:

$$-\oint_{S_c} h \, v \cdot \hat{n} \; dS = \int_{A_c} \frac{\partial h}{\partial \tau} \, dA \tag{22}$$

where A_c and S_c are the cell area and perimeters, respectively. The left hand side of the above equation is the sum of the flows out of the cell while the right hand side is the rate of change of the cell volume. The finite-difference form of this equation is:

$$\begin{aligned} F_{i,j} = {} & \frac{\Delta z_i}{2}\left(u_1 h_1 - u_4 h_4\right) + \frac{\Delta z_{i-1}}{2}\left(u_2 h_2 - u_3 h_3\right) + \\ & + \frac{\Delta \theta_j}{2}\left(v_1 h_1 - v_2 h_2\right) + \frac{\Delta \theta_{j-1}}{2}\left(v_4 h_4 - v_3 h_3\right) - \\ & - \frac{1}{4}\frac{\partial h_{i,j}}{\partial \tau}\left(\Delta z_i + \Delta z_{i-1}\right)\left(\Delta \theta_j + \Delta \theta_{j-1}\right) = 0 \end{aligned} \tag{23}$$

where $F_{i,j}$ is the error in satisfying continuity of flow in the cell centered at i,j. Although the time rate of change of film thickness has been evaluated at the center of the cell, it could have alternatively been evaluated at each of the four cell corners.

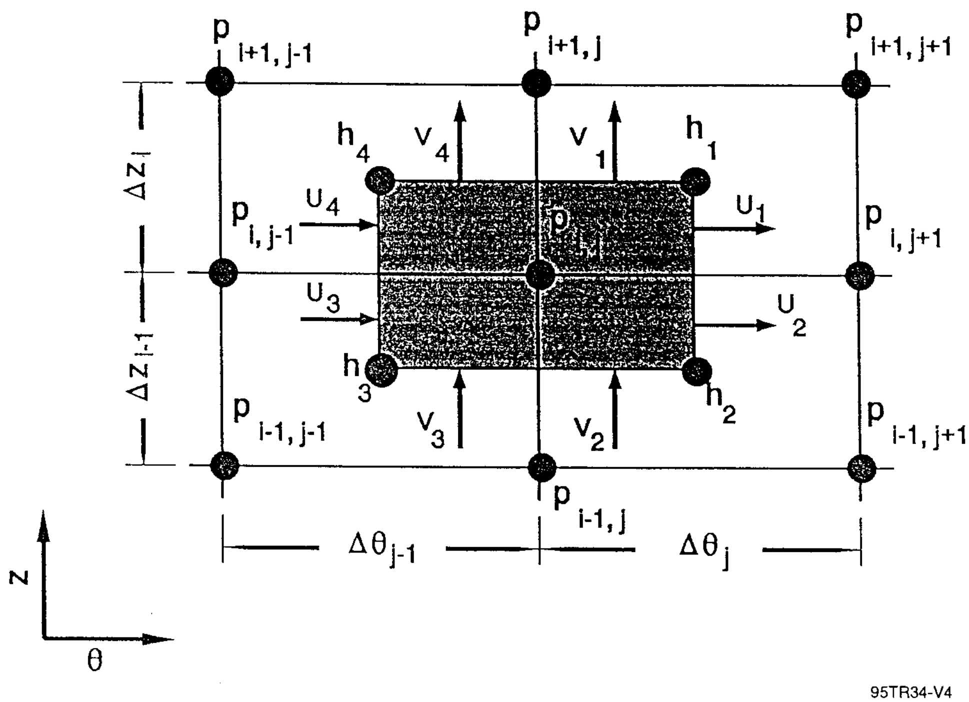

Figure 8. Flow Control Area About Grid Point I,J

When the grid point falls on a pressurized boundary, such as a pocket or seal end, the film pressure error is:

$$F_{i,j} = p_b - p_{i,j} - \Lambda_e \max(0, v_n)^2 = 0$$
$$v_n = \frac{\Sigma_{i,j}}{s_b h_{i,j}} \tag{24}$$

where p_b is the dimensionless boundary pressure*, v_n is the mean velocity of the flow that crosses the portion of the boundary perimeter that intersects the cell, and $\Sigma_{i,j}$ represents the sum of the appropriate terms in equation (23) contributing to the cell flow. Figure 9 shows an example of the cell i,j located at the right bottom corner of a pocket. In this case, the mean velocity would be evaluated as:

$$v_n = \left[\frac{\Delta z_i}{2}(u_1 h_1) + \frac{\Delta z_{i-1}}{2}(u_2 h_2 - u_3 h_3) + \frac{\Delta\theta_j}{2}(v_1 h_1 - v_2 h_2) - \frac{\Delta\theta_{j-1}}{2}(v_3 h_3) - \frac{\partial h_{i,j}}{\partial \tau}\,\frac{(\Delta z_i + \Delta z_{i-1})\Delta\theta_j + \Delta z_{i-1}\Delta\theta_{j-1}}{4} \right] \div \left[\frac{(\Delta\theta_{j-1} + \Delta z_i) h_{i,j}}{2} \right] \tag{25}$$

Equations (23) and (24) represent the finite-difference form of the continuity equation that must be solved for the pressures. The eight components of velocity used in these equations are functions of the nine pressures at or neighboring grid point i,j, and are evaluated as described in section 2.3. Following the procedure described in Reference 10, these highly nonlinear equations can be solved using the Newton-Raphson iteration method [11]. The procedure is started with an initially guessed or previously calculated pressure distribution, $\mathbf{p}_{i,j}$. The error function $\mathbf{F}_{ij}$ is then linearized about this guess in order to obtain a better approximation to the pressures $\mathbf{p}_{i,j}^{new}$:

$$F_{ij} + \sum_{\substack{k=i-1,i+1 \\ l=j-1,j+1}} \frac{\partial F_{ij}}{\partial P_{kl}} \left(P_{kl}^{new} - P_{kl} \right) = 0 \tag{26}$$

where a forward difference or a central difference may optionally be used to numerically evaluate the partial derivatives. Pressures without the superscript **new** relate to the previous or "old" approximation. If we introduce the column vector $\{\mathbf{p}_j^{new}\}$ as the **M** new pressures at the jth column of grid points, Equation (26) may be written:

$$[C^j]\{p_j^{new}\} + [E^j]\{p_{j-1}^{new}\} + [D^j]\{p_{j+1}^{new}\} = \{R^j\} \quad , \tag{27}$$

*P_l/P_o, P_r/P_o or P_p/P_o.

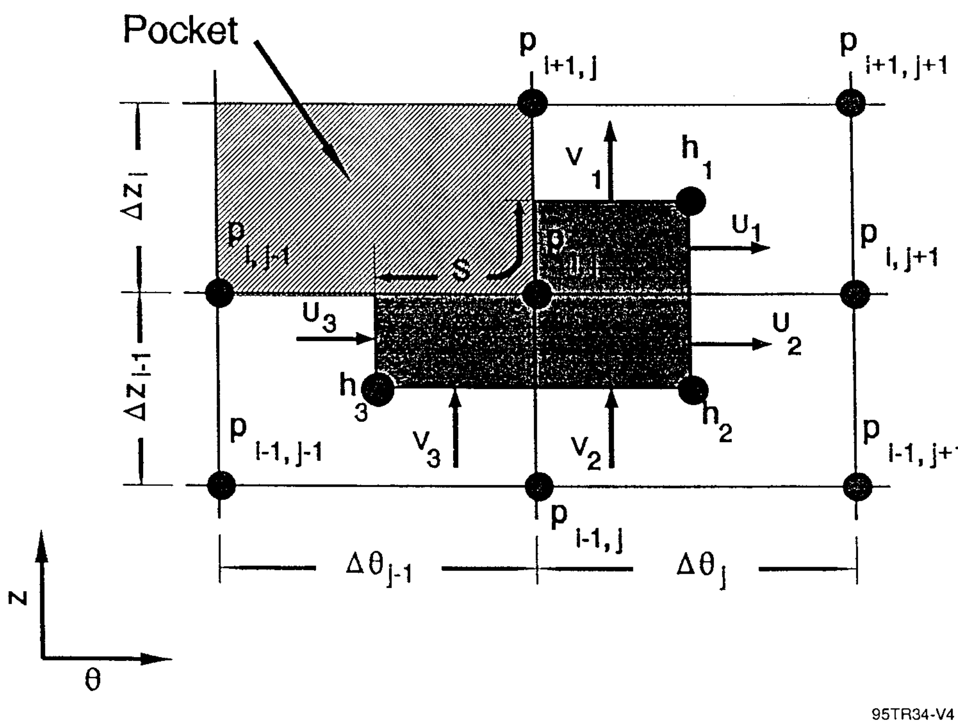

Figure 9. Example of Cell at Corner of Pocket

where $[C^j]$, $[E^j]$ and $[D^j]$ are tri-diagonal matrices whose interior elements are:

$$C^j_{i,i+k} = \frac{\partial F_{ij}}{\partial p_{i+k,j}} \;, \quad E^j_{i,i+k} = \frac{\partial F_{ij}}{\partial p_{i+k,j-1}} \;, \quad D^j_{i,i+k} = \frac{\partial F_{ij}}{\partial p_{i+k,j+1}} \;, \quad k = -1,0,1 \;; \quad i = 2,\ldots,M-1 \;.$$

The interior elements of the column vector $\{R^j\}$ are:

$$R^j_i = \sum_{k=-1}^{1} \left(C^j_{i,i+k} p_{i+k,j} + E^j_{i,i+k} p_{i+k,j-1} + D^j_{i,i+k} p_{i+k,j+1} \right) - F_{ij} \;.$$

The set of linear equations (27) that result for the next guess of pressure distribution is in a form suitable for solution by the column method which is described in detail in References 9 and 12. This method makes use of the banded nature of the equations in order to minimize computer time.

2.3 Solution of Flow Velocity

The momentum equations (16) are used in order to evaluate the velocity components from the pressure gradients. These equations may be rewritten in the generic form:

$$\begin{aligned} G_u\left[\frac{\partial p}{\partial \theta}, u, v\right] &\equiv \frac{f_j Re_j + f_b Re_b}{2} u + 12h^2 \frac{\partial p}{\partial \theta} - \left(Re_j f_j \Lambda_j + Re_b f_b \Lambda_b\right) = 0, \\ G_v\left[\frac{\partial p}{\partial z}, u, v\right] &\equiv \frac{f_j Re_j + f_b Re_b}{2} v + 12h^2 \frac{\partial p}{\partial z} = 0, \end{aligned} \qquad \textbf{(28)}$$

where the Reynolds numbers used to evaluate the friction factors are based on the *magnitude* of the local fluid velocity relative to each surface:

$$\begin{aligned} Re_j &= \frac{Re_o^* h}{12} \sqrt{(u - 2\Lambda_j)^2 + v^2}, \\ Re_b &= \frac{Re_o^* h}{12} \sqrt{(u - 2\Lambda_b)^2 + v^2}, \end{aligned} \qquad \textbf{(29)}$$

The dependence of the friction factors on velocity components orthogonal to each momentum direction couples the two momentum equations. Figure 10 is a schematic of the rectangular region between meridional grid lines i and i+1 and circumferential grid lines j and j+1. In order to preserve continuity, it is essential that the same equation be used to evaluate the velocity components for adjacent cells. That is, the velocity u_1 out of the shaded cell centered at i,j must have the same value as the velocity u_4 into the cell centered at i,j+1 (see Figure 8). This value is designated as u^- in the figure. Similarly, the velocity v_1 out of the cell i,j must

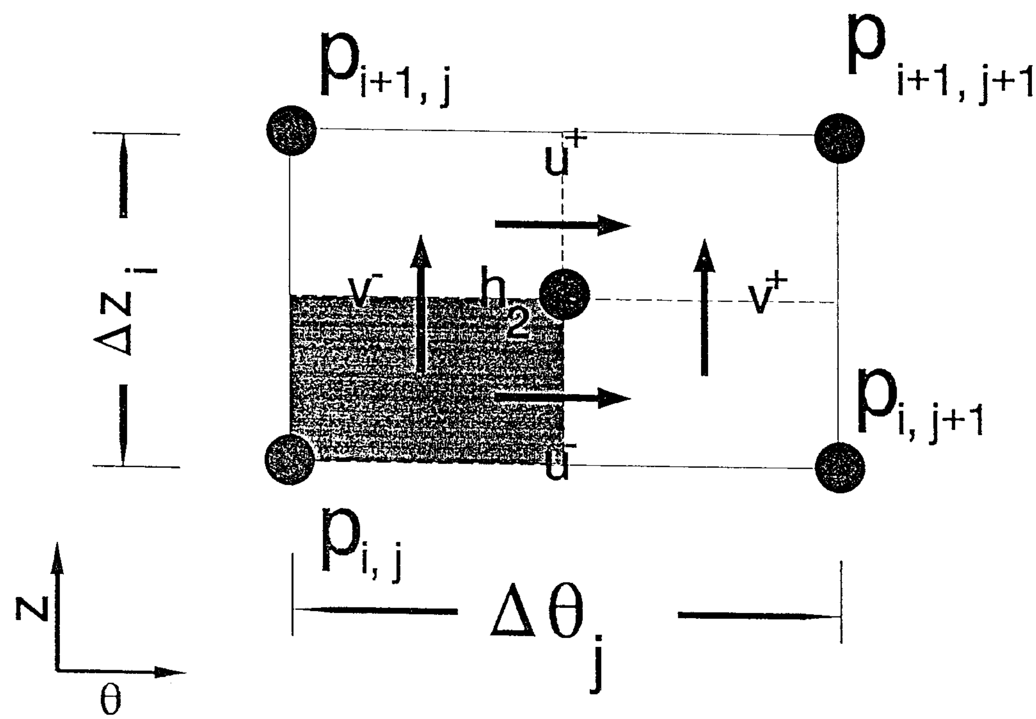

Figure 10. Schematic of Rectangular Region Between Grid Lines

be the same as v_2 into the cell at i+1,j, and is designated as v^-. This is achieved by using the average of the two corresponding orthogonal components. Thus, the component u^- is determined by the u-momentum equation:

$$G_u\left[\frac{p_{i,j+1}-p_{i,j}}{\Delta\theta_j},\ u^-,\ \frac{v^-+v^+}{2}\right]=0 \tag{30}$$

while the component v^- is determined by the v-momentum equation:

$$G_v\left[\frac{p_{i+1,j}-p_{i,j}}{\Delta z_i},\ \frac{u^-+u^+}{2},\ v^-\right]=0 \tag{31}$$

Similarly, u^+ and v^+ are determined by:

$$\begin{aligned} &G_u\left[\frac{p_{i+1,j+1}-p_{i+1,j}}{\Delta\theta_j}, u^+, \frac{v^-+v^+}{2}\right]=0 \\ &G_v\left[\frac{p_{i+1,j+1}-p_{i,j+1}}{\Delta z_i}, \frac{u^-+u^+}{2}, v^+\right]=0 \end{aligned} \tag{32}$$

Equations (30), (31) and (32) are four coupled equations that determine the velocity components from the four pressures at the corners of the rectangle between grid lines and must be solved simultaneously. This is done using an inner Newton-Raphson iteration loop. By performing the differentiation of the error functions (G_u, G_v, ...) with respect to the four unknown velocities, analytically instead of numerically, significant computer time is saved. If the velocities have not been previously calculated initial guesses may be obtained from equations (8) assuming laminar flow. Once the iterations for the velocities have converged, their values are saved to provide a good starting guess for the next time they must be calculated.

One simplification is possible by assuming that the friction factors are constant within the rectangular region and the Reynolds numbers are based on the averaged flow velocity components, $\frac{1}{2}(u^-+u^+)$ and $\frac{1}{2}(v^-+v^+)$. Although this does not uncouple the four equations, it requires less number of evaluations of the square root in equation (18). Since this assumption saves some computer time without introducing significant errors, it was chosen as the default program option. However, occasionally when the grid is not very fine and the pressure gradients vary rapidly, the iterations will diverge and the more rigorous formulation, which uses distinct friction factors for each of the four momentum equations, should be used.

If the surfaces are smooth and the housing is stationary so that the continuity equation takes the form of equation (10), the simpler formulation described in detail in Reference 10 may be used, resulting in significant reduction in computer time.

2.4 Fluid Film Load, Moment and Torque

The forces and moments on the rotor generated by the fluid film pressure distribution are obtained by integration of the pressure distribution over the cylindrical seal surface:

$$\begin{Bmatrix} F_x \\ F_y \\ M_x \\ M_y \end{Bmatrix} = \int_{-L}^{L} \int_{\theta_s}^{\theta_e} P \begin{Bmatrix} \cos\theta \\ \sin\theta \\ -Z\sin\theta \\ Z\cos\theta \end{Bmatrix} R\,d\theta\,dZ \tag{33}$$

The dimensionless form of this equation is written:

$$\begin{Bmatrix} f_x \\ f_y \\ m_x \\ m_y \end{Bmatrix} = \int_{-\frac{L}{D}}^{\frac{L}{D}} \int_{\theta_s}^{\theta_e} p \begin{Bmatrix} \cos\theta \\ \sin\theta \\ -z\sin\theta \\ z\cos\theta \end{Bmatrix} d\theta\,dz \tag{34}$$

For the face geometry, the differential of forces and moments are given by

$$d\begin{Bmatrix} F_z \\ M_x \\ M_y \end{Bmatrix} = p \begin{Bmatrix} 1 \\ -r\sin\theta \\ r\cos\theta \end{Bmatrix} dA \tag{35}$$

where the pressure p is a function of r and θ and

$$dA = r\,dr\,d\theta \tag{36}$$

The pressure in the rectangular region $\theta_j<\theta<\theta_{j+1}$, $R_i<r<R_{i+1}$ can be expressed most accurately as a bilinear function of the coordinates as:

$$p(r,\theta) = a_1 + a_2 r + a_3\theta + a_4 r\theta \tag{37}$$

where the coefficients are functions of the values of the pressure at the four corners of the rectangle:

$$
\begin{aligned}
a_1 &= \frac{\left(p_{i,j} R_{i+1} - p_{i+1,j} R_i\right)\theta_{j+1} - \left(p_{i,j+1} R_{i+1} - p_{i+1,j+1} R_i\right)\theta_j}{\left(R_{i+1} - R_i\right)\ \left(\theta_{j+1} - \theta_j\right)} \\
a_2 &= \frac{p_{i,j+1} R_{i+1} - p_{i+1,j+1} R_i - p_{i,j} R_{i+1} + p_{i+1,j} R_i}{\left(R_{i+1} - R_i\right)\ \left(\theta_{j+1} - \theta_j\right)} \\
a_3 &= \frac{\left(p_{i+1,j} - p_{i,j}\right)\theta_{j+1} - \left(p_{i+1,j+1} - p_{i,j+1}\right)\theta_j}{\left(R_{i+1} - R_i\right)\ \left(\theta_{j+1} - \theta_j\right)} \\
a_4 &= \frac{p_{i+1,j+1} - p_{i,j+1} - p_{i+1,j} + p_{i,j}}{\left(R_{i+1} - R_i\right)\ \left(\theta_{j+1} - \theta_j\right)}
\end{aligned}
\tag{38}
$$

The contribution to the fluid film forces and moments corresponding to the rectangle is then obtained by integrating equation (37):

$$
\Delta \begin{Bmatrix} F_z \\ M_x \\ M_y \end{Bmatrix} = \int_{\theta_j}^{\theta_{j+1}} \int_{R_i}^{R_{i+1}} \begin{Bmatrix} a_1 r + a_2 r^2 + a_3 r\theta + a_4 r^2 \theta \\ (-a_1 r^2 - a_2 r^3 - a_3 r^2\theta - a_4 r^3 \theta)\sin\theta \\ (a_1 r^2 + a_2 r^3 + a_3 r^2\theta + a_4 r^3 \theta)\cos\theta \end{Bmatrix} dr\, d\theta \tag{39}
$$

to obtain:

$$
\Delta \begin{Bmatrix} F_z \\ M_x \\ M_y \end{Bmatrix} = \begin{bmatrix} \Im_R^1 \Im_\theta^0 & \Im_R^2 \Im_\theta^0 & \Im_R^1 \Im_\theta^1 & \Im_R^2 \Im_\theta^1 \\ -\Im_R^2 \Im_\theta^0 & -\Im_R^3 \Im_\theta^0 & -\Im_R^2 \Im_s^1 & -\Im_R^3 \Im_s^1 \\ \Im_R^2 \Im_\theta^0 & \Im_R^3 \Im_\theta^0 & \Im_R^2 \Im_c^1 & \Im_R^3 \Im_c^1 \end{bmatrix} \begin{Bmatrix} a_1 \\ a_2 \\ a_3 \\ a_4 \end{Bmatrix} \tag{40}
$$

where

$$
\begin{aligned}
\mathfrak{I}_c^n &\equiv \int_{\theta_j}^{\theta_{j+1}} \theta^n \cos\theta \; d\theta = \left[\cos^n\theta - \theta^n \sin\theta \right]_{\theta_j}^{\theta_{j+1}}, \\
\mathfrak{I}_s^n &\equiv \int_{\theta_j}^{\theta_{j+1}} \theta^n \sin\theta \; d\theta = \left[\sin^n\theta - \theta^n \cos\theta \right]_{\theta_j}^{\theta_{j+1}}, \\
\mathfrak{I}_\theta^n &\equiv \int_{\theta_j}^{\theta_{j+1}} \theta^n \; d\theta = \frac{\theta_{j+1}^{n+1} - \theta_j^{n+1}}{n+1}, \\
\mathfrak{I}_R^n &\equiv \int_{r_i}^{r_{i+1}} r^n \; dr = r^n \; dr = \frac{R_{i+1}^{n+1} - R_i^{n+1}}{n+1}.
\end{aligned}
\tag{41}
$$

For the cylindrical geometry,

$$
d\begin{Bmatrix} F_x \\ F_y \\ M_x \\ M_y \end{Bmatrix} = p \begin{Bmatrix} -\cos\theta \\ -\sin\theta \\ z\sin\theta \\ -z\cos\theta \end{Bmatrix} R\, d\theta\, DZ \tag{42}
$$

The pressure in the rectangle ($\theta_j<\theta<\theta_{j+1}, z_i<z<z_{i+1}$) can be expressed as a linear function of the coordinates:

$$
p(z,\theta) = a_1 + a_2 z + a_3 \theta + a_4 z \theta \tag{43}
$$

where the coefficients are functions of the values of the pressure at the four corners of the rectangle:

$$a_1 = \frac{(p_{i,j}\, z_{i+1} - p_{i+1,j}\, z_i)\theta_{j+1} - (p_{i,j+1}\, z_{i+1} - p_{i+1,j+1}\, z_i)\theta_j}{(z_{i+1} - z_i)\ (\theta_{j+1} - \theta_j)}$$

$$a_2 = \frac{p_{i,j+1}\, z_{i+1} - p_{i+1,j+1}\, z_i - p_{i,j}\, z_{i+1} + p_{i+1,j}\, z_i}{(z_{i+1} - z_i)\ (\theta_{j+1} - \theta_j)}$$

$$a_3 = \frac{(p_{i+1,j} - p_{i,j})\theta_{j+1} - (p_{i+1,j+1} - p_{i,j+1})\theta_j}{(z_{i+1} - z_i)\ (\theta_{j+1} - \theta_j)} \tag{44}$$

$$a_4 = \frac{p_{i+1,j+1} - p_{i,j+1} - p_{i+1,j} + p_{i,j}}{(z_{i+1} - z_i)\ (\theta_{j+1} - \theta_j)}$$

Substituting equations (43) & (44) allows integration of (42) over the rectangle:

$$\Delta\begin{Bmatrix} F_x \\ F_y \\ M_x \\ M_y \end{Bmatrix} = R\int_{\theta_j}^{\theta_{j+1}}\int_{z_i}^{z_{i+1}} \begin{Bmatrix} -(a_1 + a_2 z + a_3\theta + a_4 z\theta)\cos\theta \\ -(a_1 + a_2 z + a_3\theta + a_4 z\theta)\sin\theta \\ (a_1 z + a_2 z^2 + a_3 z\theta + a_4 z^2\theta)\sin\theta \\ -(a_1 z + a_2 z^2 + a_3 z\theta + a_4 z^2\theta)\cos\theta \end{Bmatrix} dz\, d\theta \tag{45}$$

Defining

$$\mathfrak{I}_z^n \equiv \int_{z_i}^{z_{i+1}} z^n\, dz = \frac{z_{i+1}^{n+1} - z_i^{n+1}}{n+1} \tag{46}$$

yields

$$\Delta\begin{Bmatrix} F_x \\ F_y \\ M_x \\ M_y \end{Bmatrix} = \begin{bmatrix} -\mathfrak{I}_z^0\mathfrak{I}_c^0 & -\mathfrak{I}_z^1\mathfrak{I}_c^0 & -\mathfrak{I}_z^0\mathfrak{I}_c^1 & -\mathfrak{I}_z^1\mathfrak{I}_c^1 \\ -\mathfrak{I}_z^0\mathfrak{I}_s^0 & -\mathfrak{I}_z^1\mathfrak{I}_s^0 & -\mathfrak{I}_z^0\mathfrak{I}_s^1 & -\mathfrak{I}_z^1\mathfrak{I}_s^1 \\ \mathfrak{I}_z^1\mathfrak{I}_s^0 & \mathfrak{I}_z^2\mathfrak{I}_s^0 & \mathfrak{I}_z^1\mathfrak{I}_s^1 & \mathfrak{I}_z^2\mathfrak{I}_s^1 \\ -\mathfrak{I}_z^1\mathfrak{I}_c^0 & -\mathfrak{I}_z^2\mathfrak{I}_c^0 & -\mathfrak{I}_z^1\mathfrak{I}_c^1 & -\mathfrak{I}_z^2\mathfrak{I}_c^1 \end{bmatrix} \begin{Bmatrix} a_1 \\ a_2 \\ a_3 \\ a_4 \end{Bmatrix} \tag{47}$$

The differential of torque transmitted from the housing to the rotor is given by the cross product of the position vector $\vec{r}$ and the shear traction vector acting on the housing $\vec{t}$:

$$\vec{T} = T\hat{e}_z = \iint_{A_f} \boldsymbol{r} \times \vec{t}\, dA$$

$$= R \iint_{A_f} \hat{e}_r \times (\bar{\tau} \bullet \hat{e}_r)\, dA \tag{48}$$

$$T = \frac{P_o R^2}{2C_o} \iint_{A_f} \{ h\frac{\partial p}{\partial \theta} - \frac{f_j R_j (u - 2\Lambda_j) - f_b R_b (u - 2\Lambda_b)}{72h} \}\, d\theta\, dZ$$

For laminar regime, $f_j Re_j = f_b Re_b = 12$, and the equation simplifies to:

$$T = \frac{P_o R^2}{2C_o} \iint_{A_f} \{ h\frac{\partial p}{\partial \theta} - \frac{\Lambda_j - \Lambda_b}{3h} \}\, d\theta\, dZ \tag{49}$$

The power loss due to the difference in velocities across the two surfaces is obtained by the dot product of this torque with the relative velocity:

$$P = T(\omega_b - \omega_j)$$

$$= \frac{P_o R^2}{2C_o} \iint_{A_f} \{ h\frac{\partial p}{\partial \theta} - \frac{f_j R_j (u - 2\Lambda_j) - f_b R_b (u - 2\Lambda_b)}{72h} \} (\Lambda_j - \Lambda_b)\, d\theta\, dZ \tag{50}$$

2.5 Stiffness and Damping Coefficients

Defining $\mathbf{W}$ to be a generalized vector of forces and moments generated by the fluid film pressure and $\vec{\mathbf{r}}$ to be a generalized vector of lateral and angular displacements:

$$W = \begin{Bmatrix} f_x \\ f_y \\ m_x \\ m_y \end{Bmatrix} \quad r = \begin{Bmatrix} \varepsilon_x \\ \varepsilon_y \\ \alpha \\ \beta \end{Bmatrix} \quad \dot{r} = \frac{\partial}{\partial \tau} \begin{Bmatrix} \varepsilon_x \\ \varepsilon_y \\ \alpha \\ \beta \end{Bmatrix} \tag{51}$$

the matrices of stiffness and damping coefficients can be written:

$$k_{ij} = -\frac{\partial W_i}{\partial r_j} \qquad b_{ij} = -\frac{\partial W_i}{\partial \dot{r}_j} \tag{52}$$

where the subscripts i and j range over x, y, α and β. These coefficients are evaluated by numerical differentiation of $\mathbf{W}$, using a forward difference. For example:

$$K_{y\alpha} = \frac{F_y(\epsilon_x, \epsilon_y, \alpha + \delta, \beta) - F_y(\epsilon_x, \epsilon_y, \alpha, \beta)}{\delta} \tag{53}$$

2.6 Solution of Rotor Position and Pocket Pressures

If the rotor position is specified, equation (51) is used to solve for the fluid film forces and moments in terms of the calculated pressure field. Similarly, if the pocket pressures are specified, equation (12) is used to solve for the orifice size in terms of the supply pressure and calculated pocket flow.

On the other hand, if externally applied loads and moments on the rotor ($\mathbf{f_{xg}}$, $\mathbf{f_{yg}}$, $\mathbf{m_{xg}}$ **and** $\mathbf{m_{yg}}$) are specified they must be balanced by the fluid film forces to maintain static equilibrium.

Similarly, once the orifice size is specified, equation (12) must be satisfied by the pressure in each pocket. The global set of equations that must be satisfied by the rotor displacements and pocket pressures are:

$$
\begin{aligned}
f_x(r) &= -f_{xg} \\
f_y(r) &= -f_{yg} \\
m_x(r) &= -m_{xg} \\
m_y(r) &= -m_{yg} \\
p_s - p_{p1} &= sng(q_{r1})\,\Lambda_{r1}\,(q_{r1})^2, \quad \text{for pocket } 1, \\
p_s - p_{p2} &= sng(q_{r2})\,\Lambda_{r2}\,(q_{r2})^2, \quad \text{for pocket } 2, \text{ etc.}
\end{aligned}
\tag{54}
$$

The vector $\vec{r}$ can now be redefined to include the pocket pressures and a generalized vector of errors in forces, moments and pocket pressures $\vec{W}_e$ can be defined:

$$
r = \begin{Bmatrix} \varepsilon_x \\ \varepsilon_y \\ \alpha \\ \beta \\ p_{p1} \\ p_{p2} \\ \vdots \end{Bmatrix} \qquad W_e = \begin{Bmatrix} f_x + f_{xg} \\ f_y + f_{yg} \\ m_x + m_{xg} \\ m_y + m_{yg} \\ p_s - p_{p1} - sgn(q_{r1})\,\Lambda_{r2}(q_{r1})^2 \\ p_s - p_{p2} - sgn(q_{r2})\,\Lambda_{r2}(q_{r2})^2 \\ \vdots \end{Bmatrix}
\tag{55}
$$

Solution of the global equations is performed by Newton-Raphson iterations, as follows:

$$
W_e + \left[\frac{\partial W_e}{\partial r}\right]\left(r^{new} - r \right) = 0
\tag{56}
$$

where, as before, the superscript **new** indicates the newer values of the vector $\vec{r}$.

3.0 SAMPLE PROBLEMS FOR CODE ICYL

A number of sample problems were completed to demonstrate the behavior and various features of the computer code. They are intended primarily for illustration and do not necessarily represent recommended seal designs. Table 1 summarizes the mesh size and approximate execution times (on a 20 MHz 386 PC), as well as the specified and computed variables.

The complete input file is included at the top of the output file for each case. The filenames used in the samples all used the prefix icyl. For example, EX1 used *fname* = icylEX1.

Samples EX1, EX2, and EX3 were selected with a coarse (5 x 11) mesh covering a 90° sector in order to demonstrate the use of pressurized pockets and iterations for rotor position within a reasonable execution time. A pocket with a supply pressure of 100 psi was centered on the seal sector modeled.

Sample **EX1** contained two cases. In the first case, the pocket pressure was specified as 50 psi, resulting in an orifice diameter of 0.0137 in. calculated by the program. Both components of the resulting fluid film force are equal and the moments are zero, as would be expected at the concentric position. In the second case, the rotor was moved with eccentricity ratio of $\varepsilon_x = 0.1$ and given a misalignment ratio of $\beta = 0.1$ about the y-axis. With the value of orifice diameter already assigned from the first case, the pocket pressure and forces rise slightly, generating non-zero moments.

In sample **EX2**, external forces and moments equal to the negative of those resulting in EX1 were specified, in order to have the program iterate for the rotor radial and angular positions. Five unknowns, the four displacement components (ε_x, ε_y, α, and β) as well as the pocket pressure, are iterated for simultaneously. The initial pressure distribution was read from the converged values of EX1. Since the iteration was begun at the concentric position where the orifice was sized, the pocket flow error was zero and increased when the rotor was moved in the first iteration, causing the run to abort. When the limit on diverging iterations was increased to 2, the iterations converged in only 3 iterations to within a small error of values expected ($\varepsilon_x = 0.1$, $\beta = 0.1$).

In sample **EX3**, an axial taper of ±30% of the clearance from end to end was superimposed. In this sample, the program was asked to find the angular rotor position such that no external moments were required, while the rotor eccentricity was varied, using $\varepsilon_x = 0.1$, 0.3 and 0.5 for the first, second, and third cases, respectively. The results show that as the eccentricity is increased in the x-direction, the rotor twists about the y-axis in order for the moments generated by the film to be zero, resulting in $\beta = 0.050$ and 0.17 at $\varepsilon_x = 0.1$ and 0.3, respectively. The case of $\varepsilon_x = 0.5$ resulted in a negative film thickness with the appropriate error message and recommended user action:

- Reduce the specified applied forces/moments
- Reduce the specified eccentricity/misalignment.

The resulting film thickness and pressure distributions for sample EX3 are shown in Figures 11 and 12, respectively.

Table 1. Summary of Sample Cases for Code ICYL

Case	Mesh Size	ISYM	Variable Found*	Variable Specified	App.exec time**	Features
EX1	5x11	0	dorif, P_{pock}	P_{pock}, E_x, dorif	4.6 min	1-pocket
EX2	5x11	0	$\epsilon_x, \epsilon_y, \alpha, \beta, P_{pock}$	F_x, F_y, M_x, M_y, dorif	11.6 min	1-pocket
EX3	5x11	0	α, β, P_{pock}	M_x, M_y, dorif	6.2 min	Tapered pocket
F3	9x61	1	-	all	29 min	Raleigh-step
F4	7x61	0	-	all	7.8 min	Axial taper
F9	5x73	1	K,B	all (3 preloads)	1.6 hrs	3-lobe
I1	5x61	1	dorif	P_{pock}	7 min	4-pocket
I2	5x61	1	P_{pock}, K	ϵ_x, dorif	1.8 hrs	4-pocket
I3	5x61	1	$\epsilon_x, \epsilon_y, P_{pock}$	F_x, F_y, dorif	1.9 hrs	4-pocket
I4	9x61	0	K, B, P_{pock}	ϵ_x, α, dorif	7.7 hrs	4-pocket
I5	11x61	0	dorif	P_{pock}	5.2 min	8-pocket
I6	11x61	0	P_{pock}	dorif, ϵ_x, α	3.1 hrs	8-pocket
015	5x31	0	K,B	all	1 hr 45 sec	Roughness

* K,B indicate whether stiffness, damping coefficients were requested.
** on an IBM PS/2 model 70 (386 20-Mhz) computer.

95TR34-V4

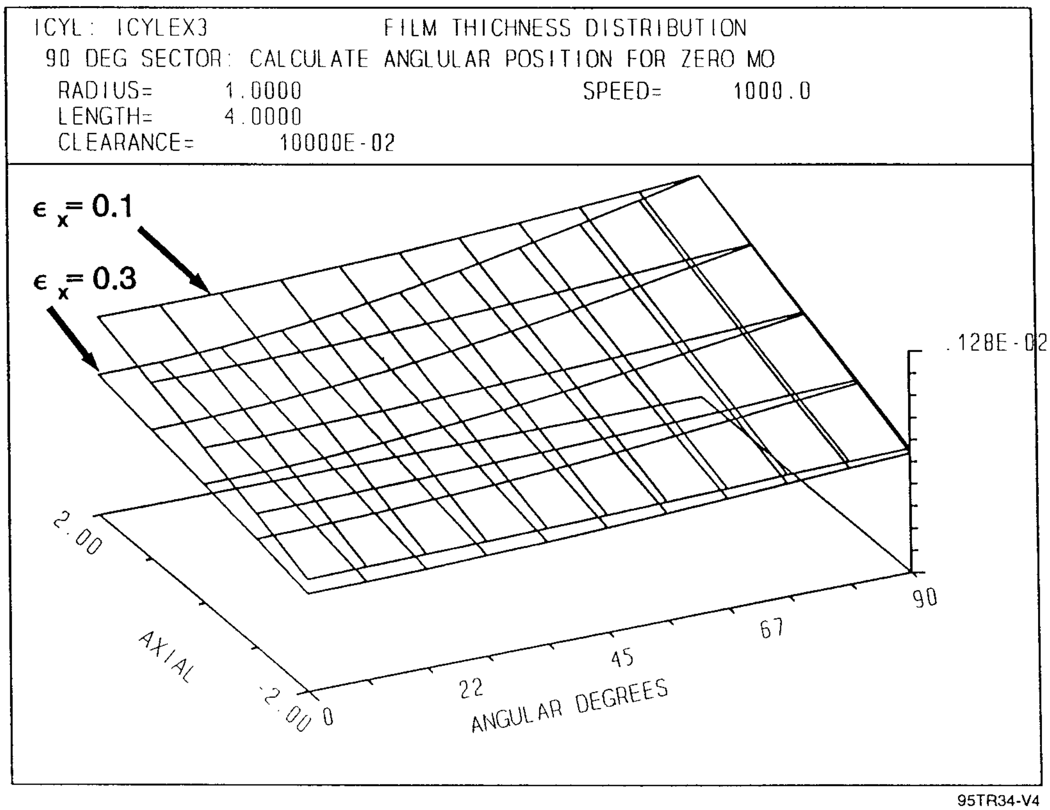

Figure 11. Film Thickness Distribution for Sample EX3

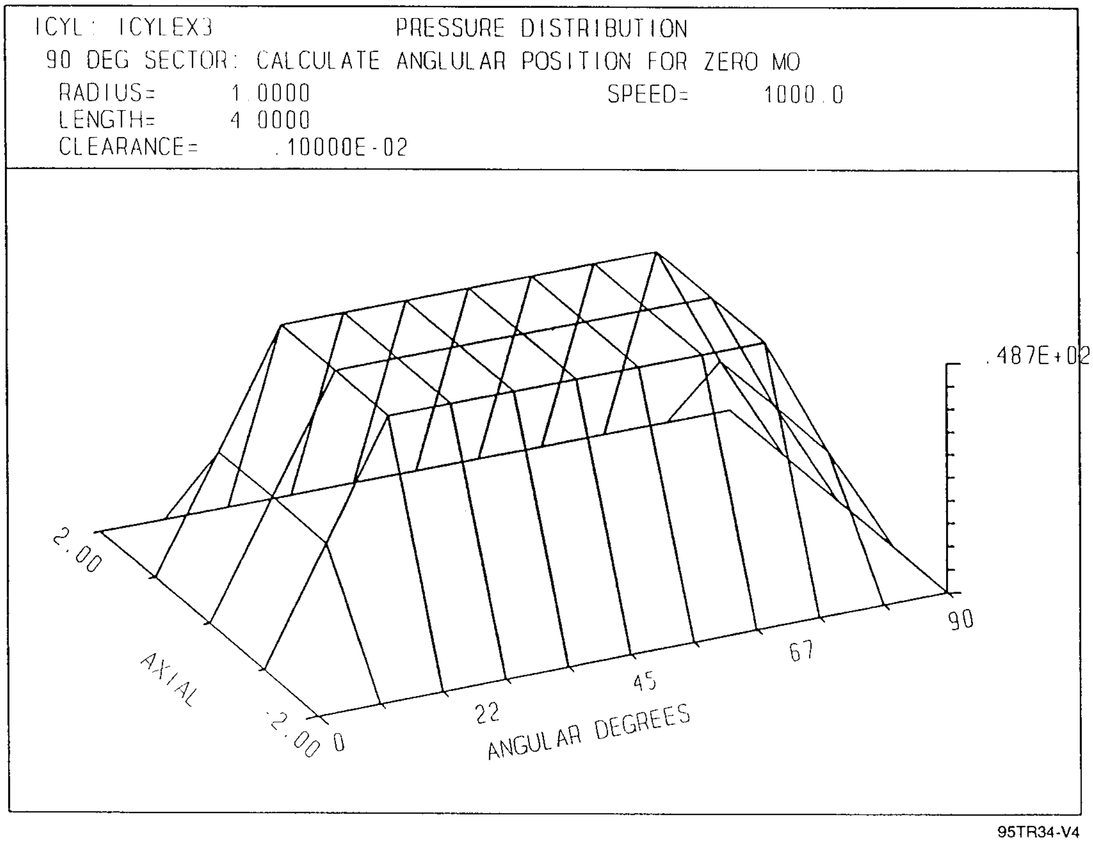

Figure 12. Pressure Distribution for Sample EX3

Sample **F3** shows a 120° sector with a Raliegh step of linearly varying depth. The resulting film thickness and pressure distributions are shown in Figures 13 and 14, respectively. Sample **F4** shows a 120° sector with an axial taper in the right half ($4<i<7$) of 0.001 in. Since two fewer intervals were used in the axial direction than in the previous cases, and since half as many iterations were required for the pressure distributions, the execution time was reduced from about 29 to 8 minutes. The resulting film thickness and pressure distributions are shown in Figures 15 and 16, respectively.

Sample **F9** is that of a full 360° seal with three 60° lobes. The dynamic coefficients were requested as the preload was increased from 0.1 to 0.3 in the middle case, to 0.8 at the last case. The resulting film thickness and pressure distributions are shown in Figures 17 and 18, respectively.

Samples I1 through I14 are more realistic models since they represent the full circumference. In sample **I1**, the program takes about 7 minutes to calculate the orifice diameter for given pocket pressures. The resulting pressure distribution is shown in Figure 19. Sample **I2** is the same as I1 except that the eccentricity and orifice diameter were prescribed, requiring the program to solve for the four pocket pressures. The resulting film thickness and pressure distributions are shown in Figures 20 and 21, respectively. In sample **I3**, the orifice diameter as well as the radial force were prescribed, requiring the program to solve for the radial position as well as the pocket pressures.

Sample **I4** shows the dynamic increase in execution time with the number of axial grid lines, M. Sample I1 is a model of only half of the seal, symmetry imposed, at the concentric position with the pocket pressures specified. This run executes in less than 7 minutes in spite of the 5 x 61 mesh. Sample I4 is a model of the full axial length (ISYM = 0), with an 11 x 61 mesh, in which non-zero ε_x, α and orifice size are specified and all 32 dynamic coefficients are requested. This run took 7.7 hours to execute. Calculations for each of these coefficients require convergence of the outer iteration loop with four unknown pocket pressures.

Samples I5 and I6 are models representing the full circumference and length with two rows of 4 pockets. The orifice size is calculated in the concentric aligned position in I5 while I6 calculates what happens when the rotor is displaced to the $\varepsilon_x = 0.4$ position and rotated about the x-axis by $\alpha = 0.4$. For I5, the resulting pressure distribution is shown in Figure 22. For I6, the film thickness and pressure distributions are shown in Figure 23 and Figure 24, respectively.

Sample **O15** is a case of a plain cylindrical seal with increasing housing wall roughness. The wall roughness (ROUGHB) was varied from 1×10^{-6} to 1×10^{-3} in. in a logarithmic scale. This input was used to generate the top curve of critical mass versus roughness shown in Figure 25. The stabilizing effect of housing roughness is more pronounced at the higher pressures due to the increased effect of inlet inertia.

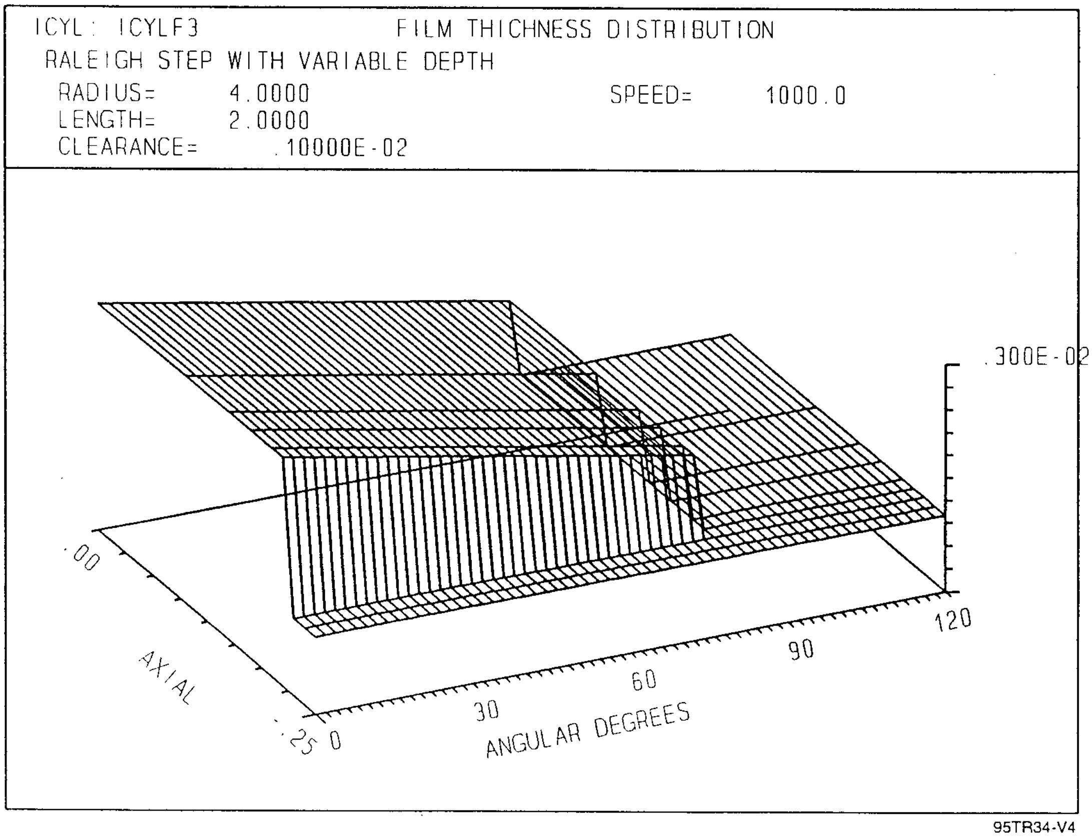

Figure 13. Film Thickness Distribution for Sample F3

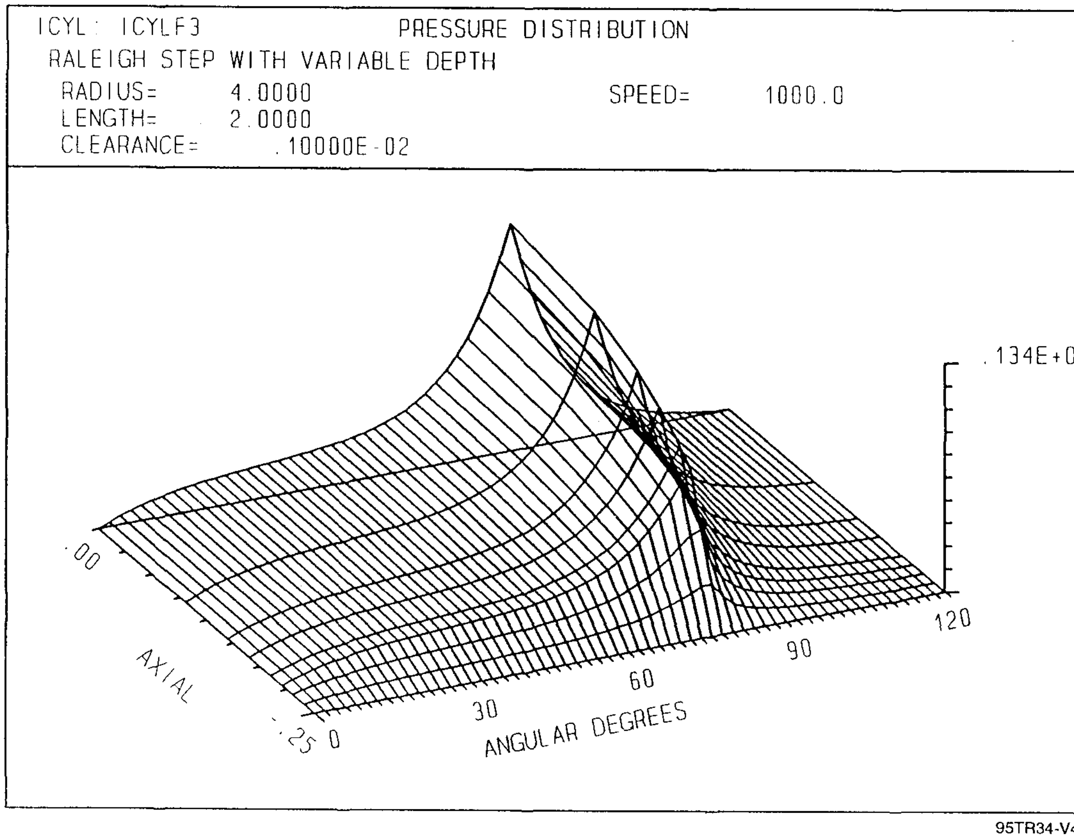

Figure 14. Pressure Distribution for Sample F3

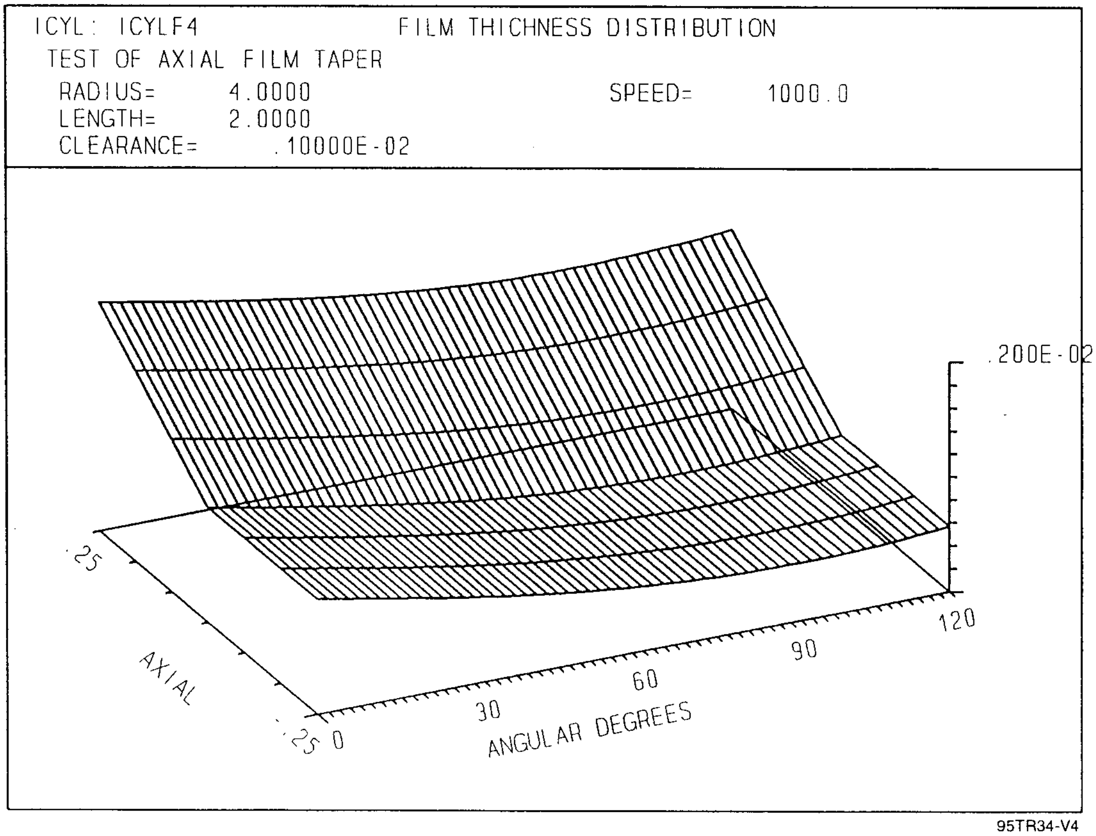

Figure 15. Film Thickness Distribution for Sample F4

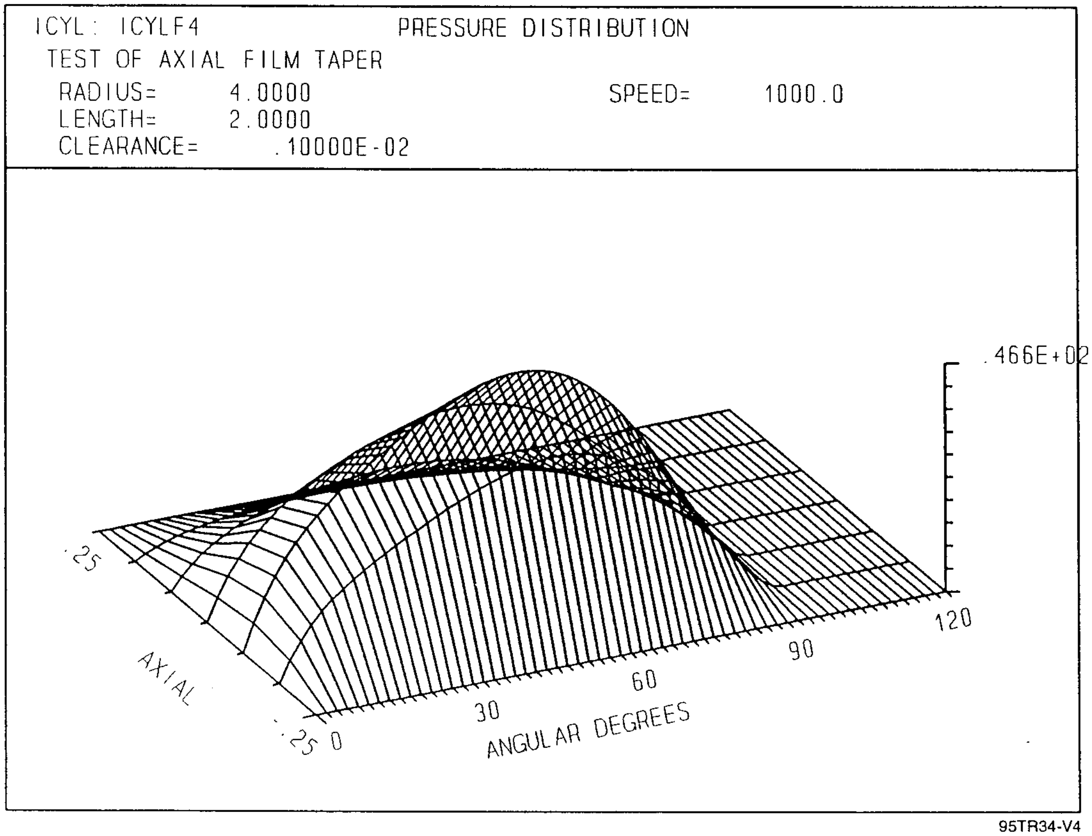

Figure 16. Pressure Distribution for Sample F4

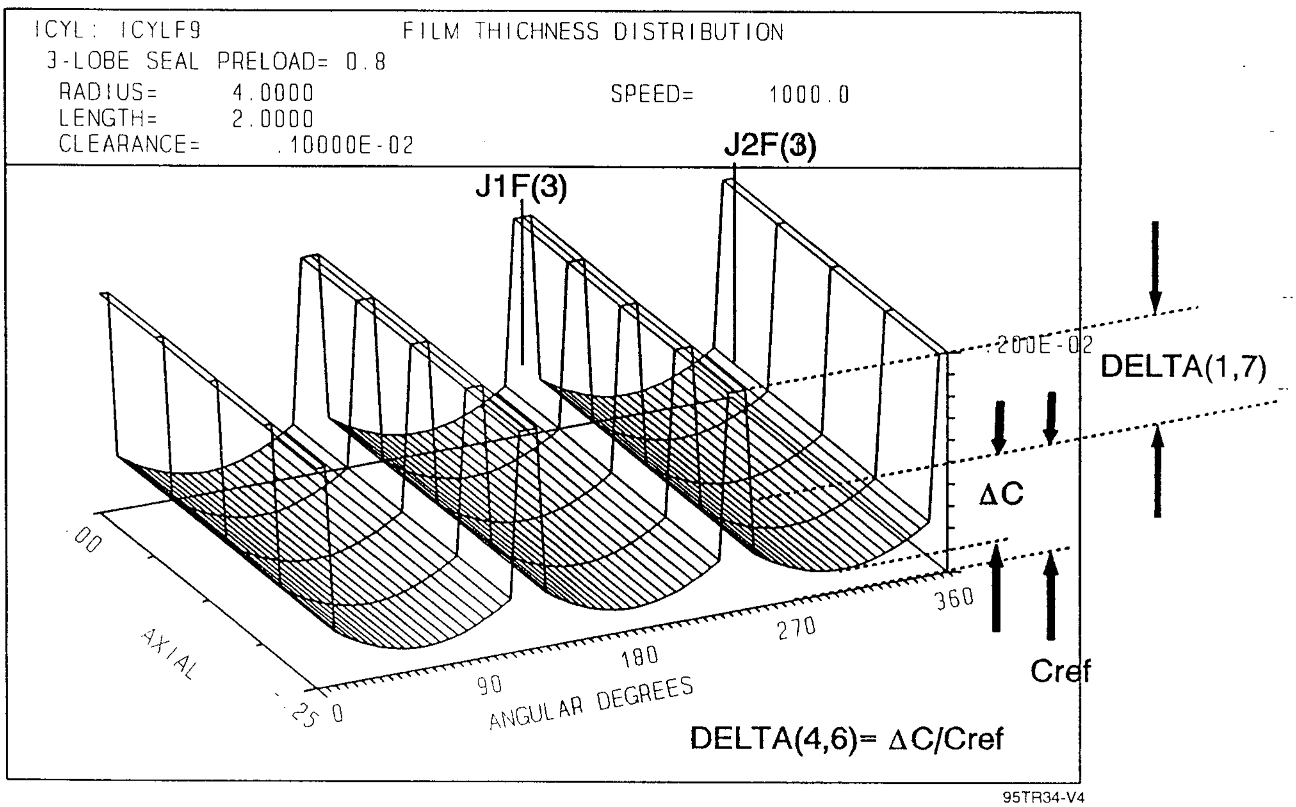

Figure 17. Film Thickness Distribution for Sample F9

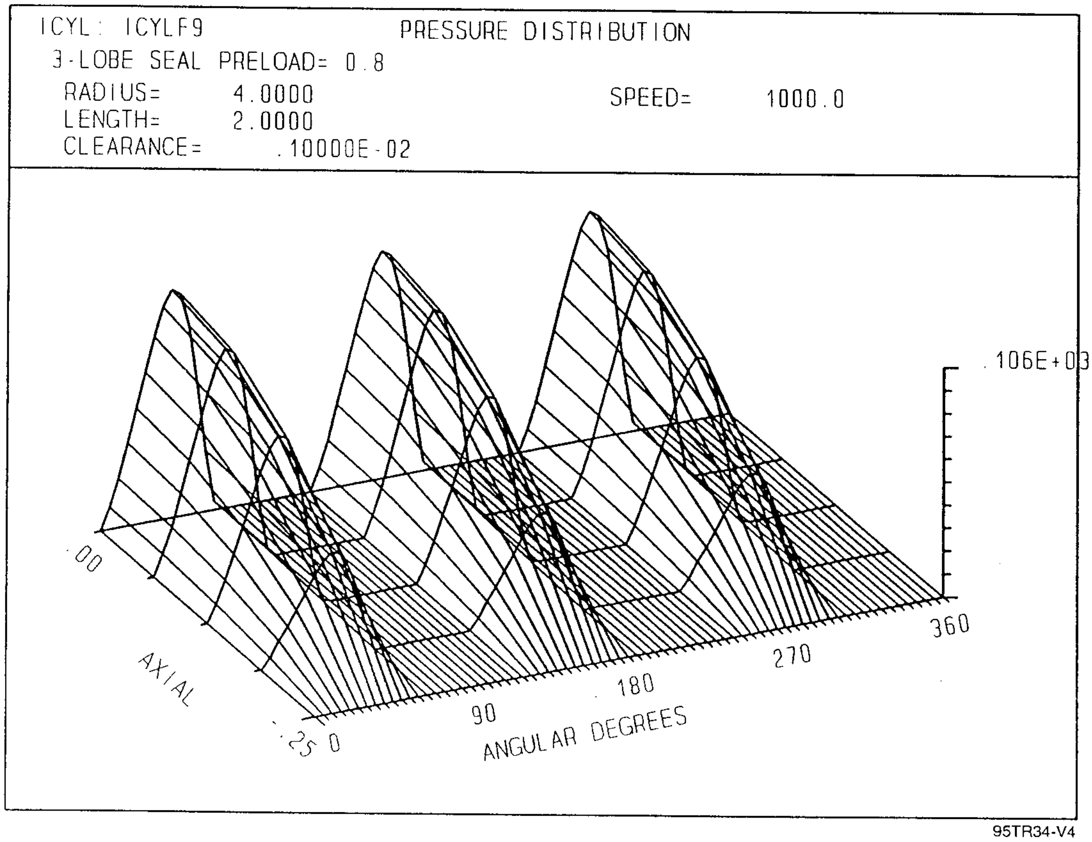

Figure 18. Pressure Distribution for Sample F9

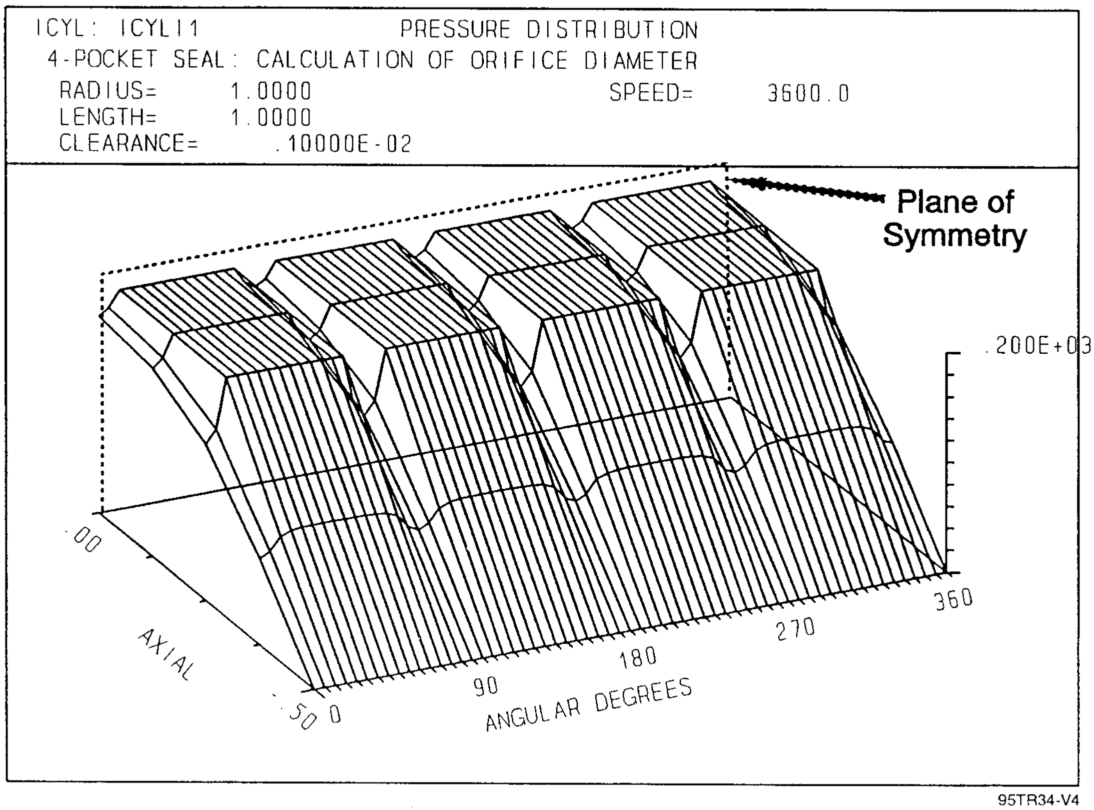

Figure 19. Pressure Distribution for Sample I1

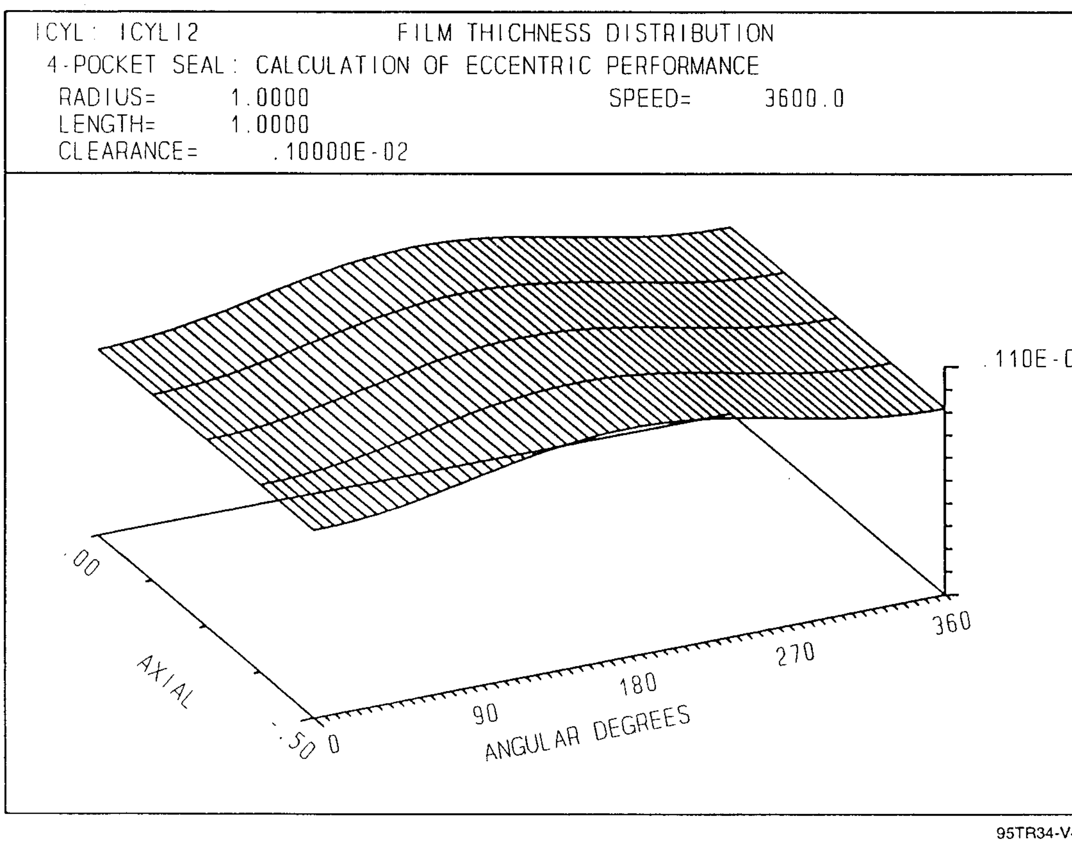

Figure 20. Film Thickness Distribution for Sample I2

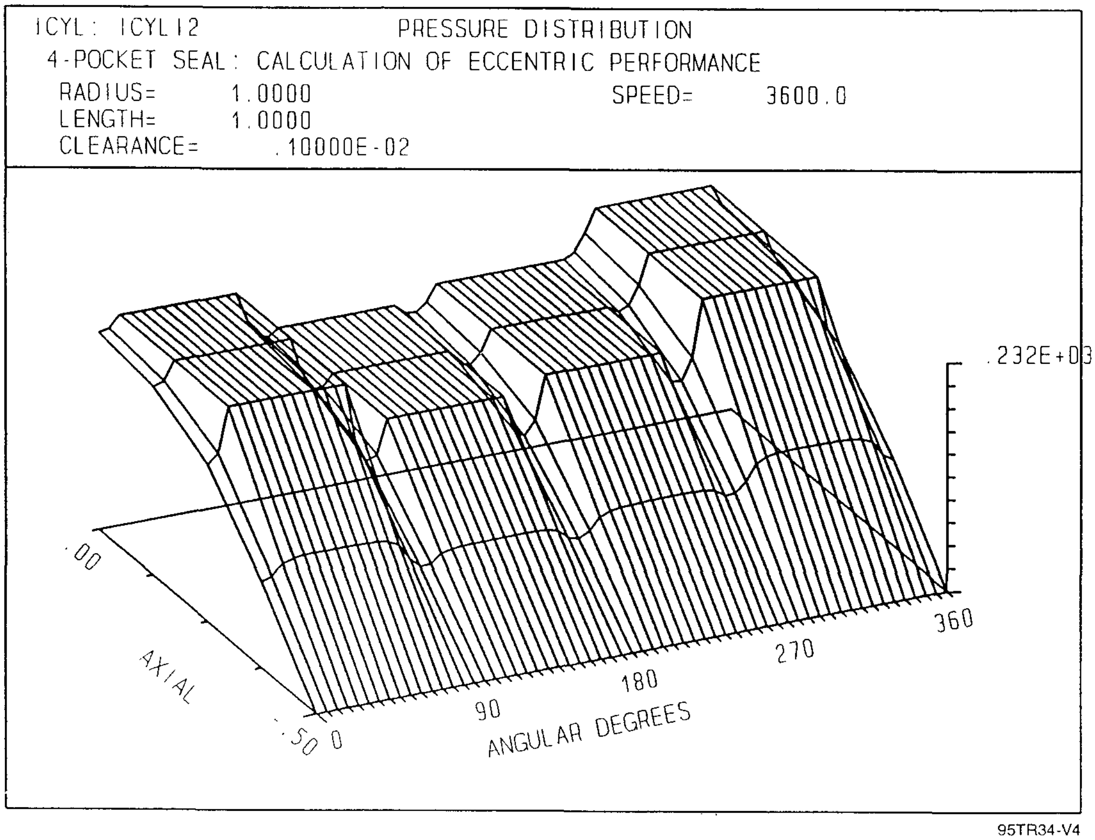

Figure 21. Pressure Distribution for Sample I2

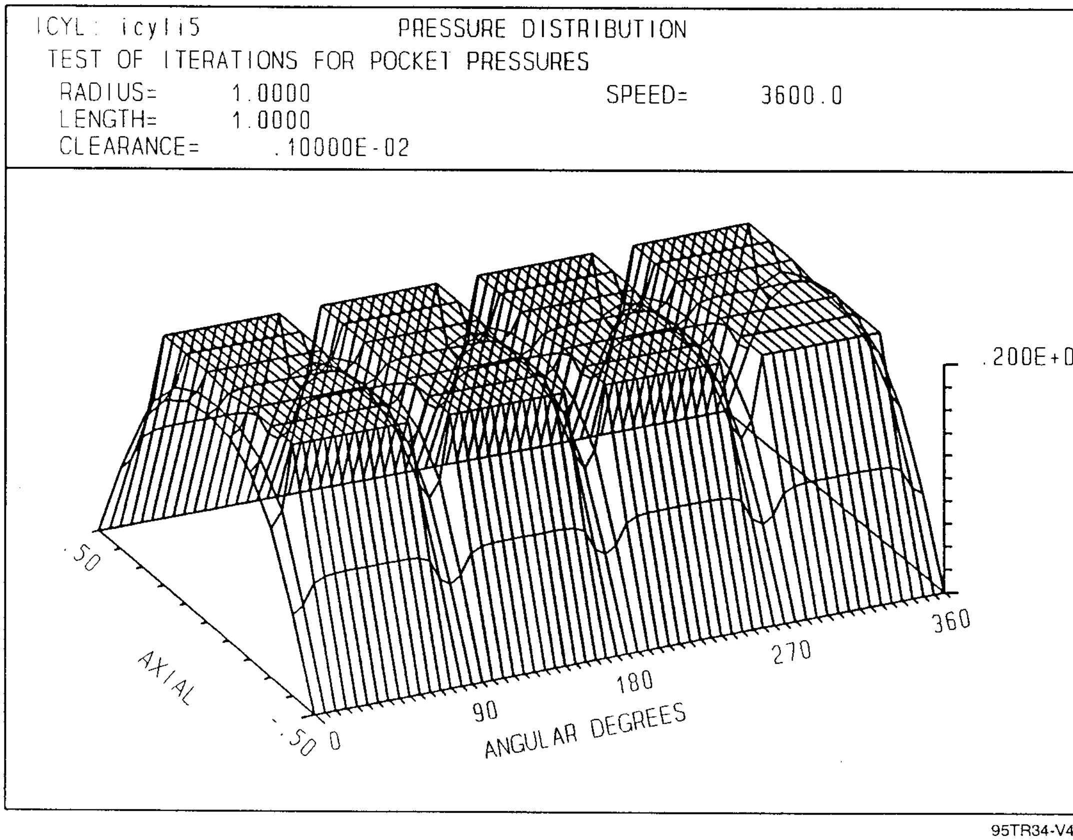

Figure 22. Pressure Distribution for Sample I5

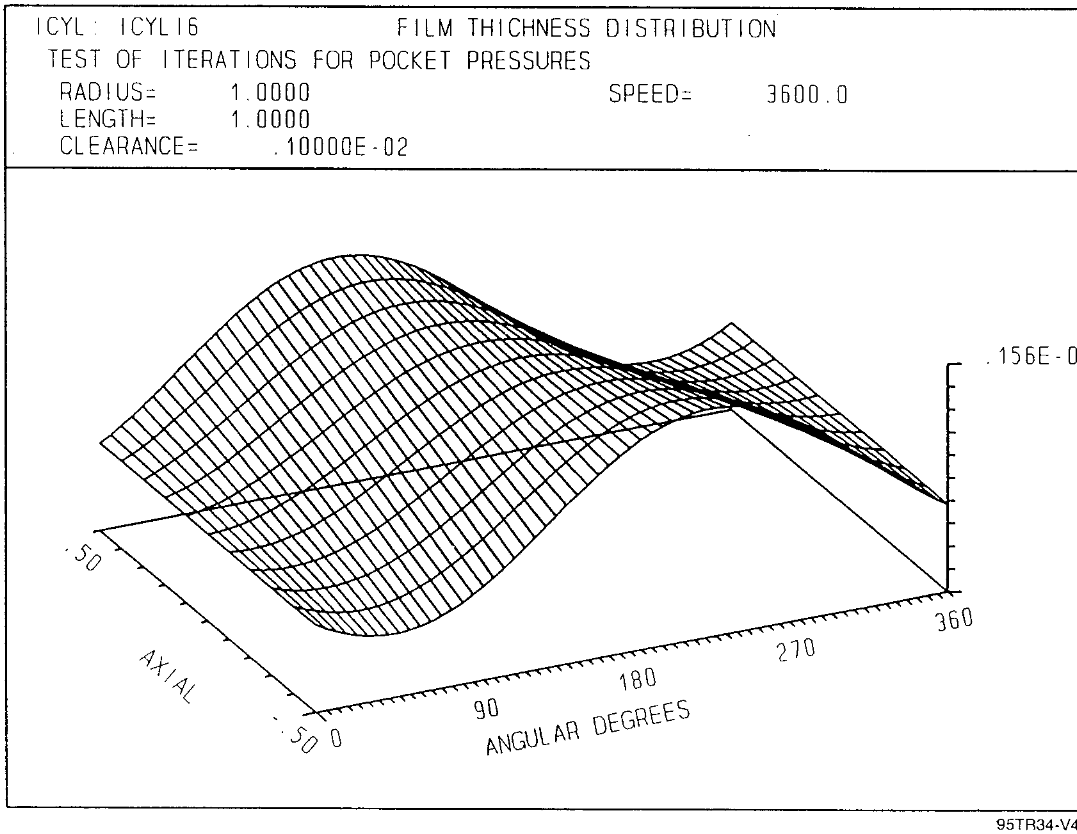

Figure 23. Film Thickness Distribution for Sample I6

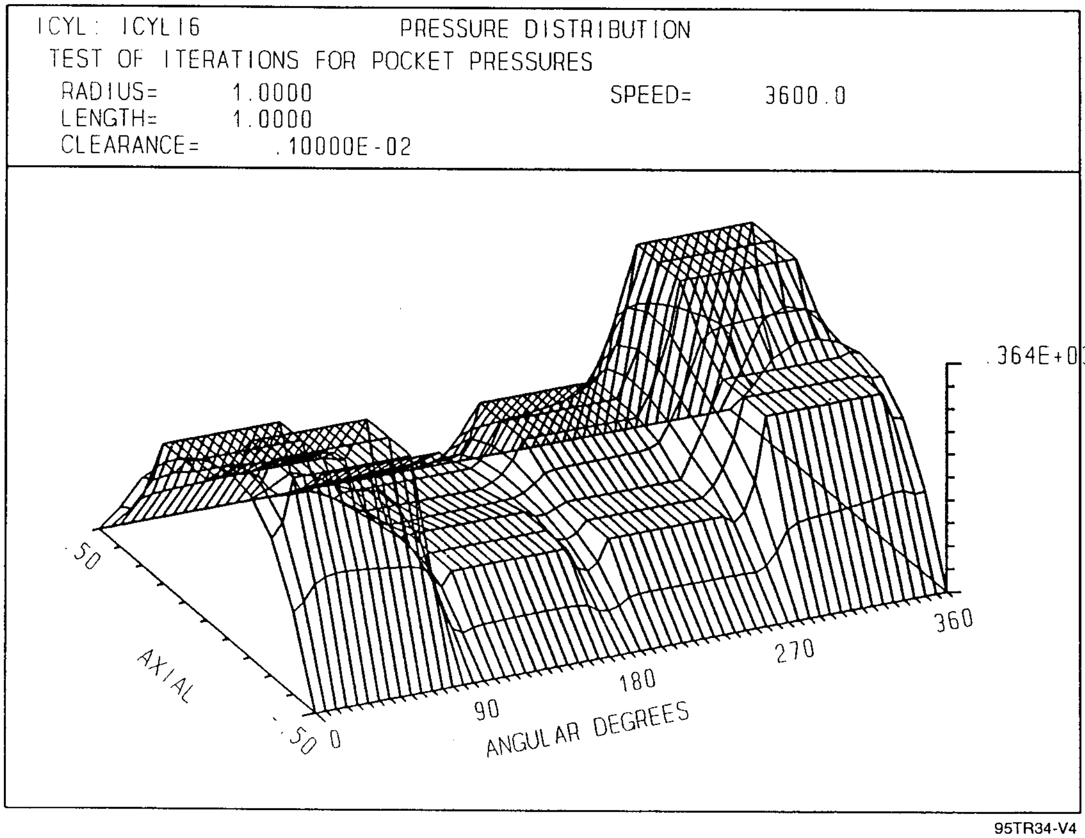

Figure 24. Pressure Distribution for Sample I6

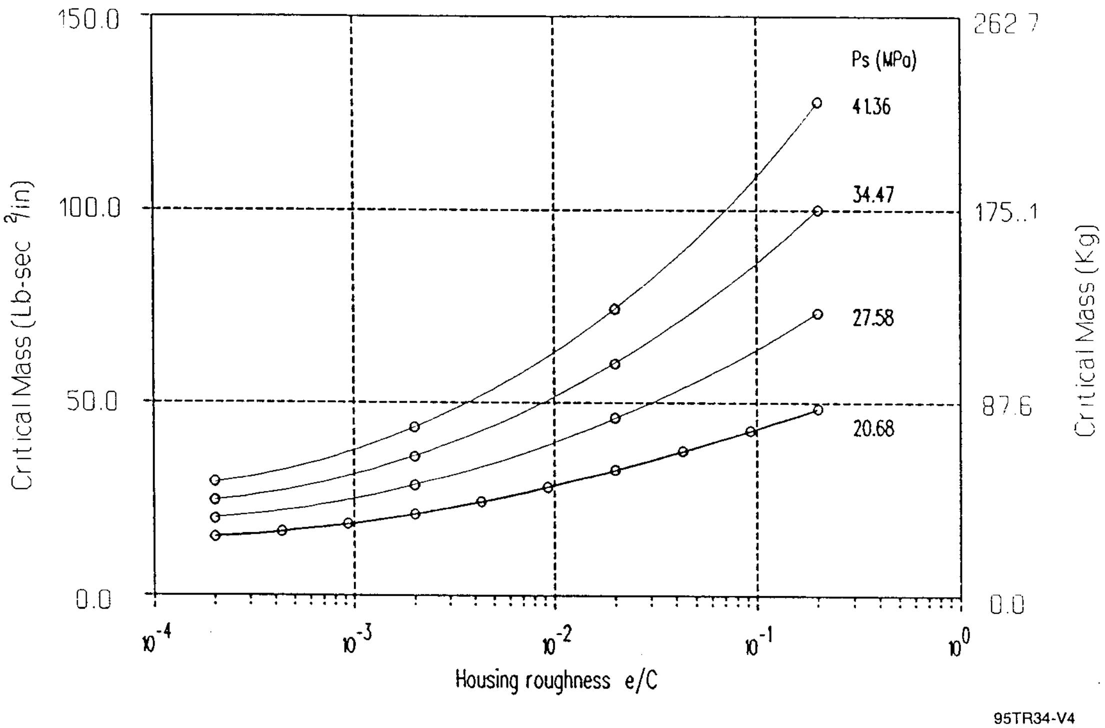

Figure 25. Critical Mass Versus Housing Roughness

4.0 SAMPLE PROBLEMS FOR CODE IFACE

A number of sample problems were completed to demonstrate the behavior and various features of the computer code. They are intended primarily for illustration and do not necessarily represent recommended seal designs. Table 2 summarizes the mesh size, approximate execution times (on a 33 MHz 486 PC) as well as the specified and computed variables.*

Sample **1** uses a coarse mesh, variable in both directions, to represent a 50° sector with a film thickness that is tapered circumferentially by 1 mil. This sample demonstrates how different input variables control the film thickness distribution. The left bottom corner point increases the film from the reference clearance to 2 mils. DELTA(3,1) (see Figure 5) then decreases the film thickness by 1 mil over the circumferential extent. The axial eccentricity ratio (EX= -0.1) decreases the clearance distribution by 10% of CREF. The model is located in the first quadrant, so the resulting pressure distribution produces a positive moment about the x axis and a negative one about the y axis. The resulting film thickness distribution is shown in Figure 26 and the pressure is shown in Figure 27.

Sample **2A** specifies a geometry that is repeated circumferentially every 120°. A zero pressure is specified at the first two grid lines of each pad while the rest of the pad's film thickness is tapered. The prescribed external force and moments were obtained from the negative of the results of a similar case at ε_z=0.2, α=0.5 and β=0. In sample 2A, the program iterates on the position, starting from zero guess values, since Ex, ALFA or BETA were not prescribed, and converges on ε_z = 0.2, α = 0.500002, and a near zero β in 4 outer loop iterations. The resulting film thickness distribution is shown in Figure 28 and the pressure is shown in Figure 29.

Samples 3A, 3B and 3C are used to illustrate the steps that would be used in calculating the performance of a hydrostatically supported, 4-pocket face seal. A variable mesh is used to describe the geometry of ¼ of the circumference between θ = 0 and 90° from the x-axis. One pocket with a supply pressure of 1000 psi is centered on the section modeled. Pressures of 100 and 200 psi are prescribed at the inner and outer radii. Periodic circumferential boundary conditions and 4 pads are specified to generate the geometry in the remaining three quadrants.

In sample **3A**, sizing of the orifice diameter is performed with pocket pressures at 500 psi and an aligned rotor. Although the ¼ model corresponding to one pocket would be sufficient for the orifice calculation, the full model was required in this case in order to calculate the angular mode stiffness and damping coefficients. The output indicates an orifice diameter of 0.069 in., a total flowrate of 9 in.^{3}/s, and a fluid film axial force of 7,376 lbf. The direct axial stiffness is K_{zz}=12.7x10^6 lb/in. and the direct angular stiffness and damping coefficients are 33.2x10^6 lb-in./rad and 29.6x10^3 lb-in./rad.

*K and B indicate calculation of stiffness and damping coefficients.

Table 2. Summary of Sample Cases

Case	Mesh size MxN	Variables specified	Variables calculated	NPADS	run time (sec)	features
1	5x11	EX, ALFA			3.75	variable grid, DELTA(1,1)
2A	5x31	FXG, MXG, MYG	EX,ALFA, BETA	3	125	prescribed force & moments, DELTA(5,1)
3A	7x41	PPOCK	DORIF, K,B	4	404	4-pocket, calculation of orifice & coefficients
3B	7x41	DORIF, EX,BETA	PPOCK	4	352	4-pocket, prescribed displacements
3C	7x41	DORIF, FXG, MXG,MYG	PPOCK, EX, ALFA,BETA	4	566	4-pocket, prescribed force & moments, pressures read
13	9x37		K, B	4	1093	preloaded pads, roughness multiple cases, DELTA(4,1)
17	9x65	ALFA		8	103	8 Rayleigh steps
15A	10x61	PPOCK	DORIF, K,B	4	2115	4-pocket with XKE=1
15B	10x61	DORIF, EX, MXG, MYG	ALFA,BETA, PPOCK	4	1368	4-pocket finding angular position, pressures read

95TR34-V4

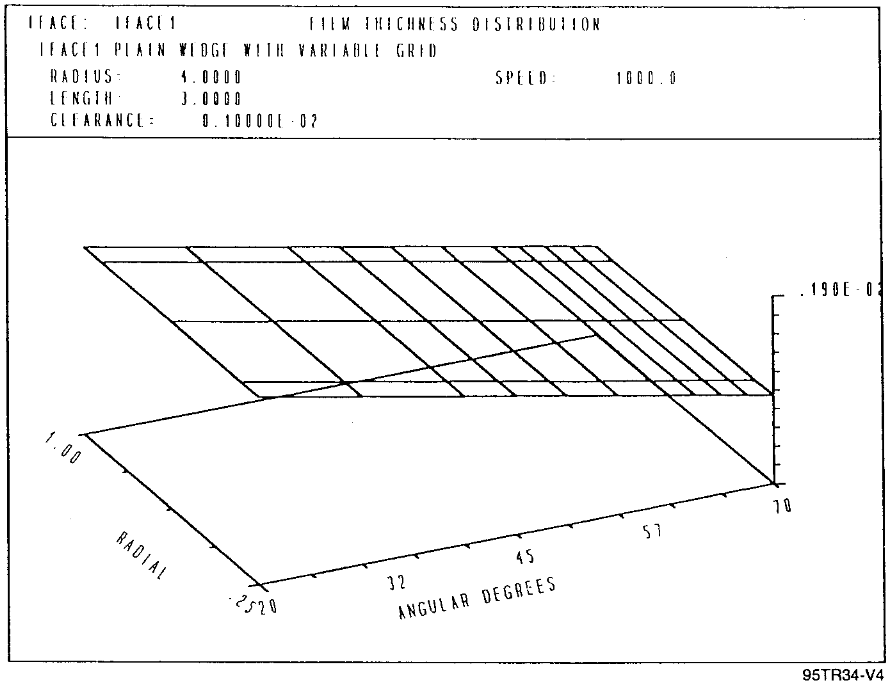

Figure 26. Film Thickness Distribution for Sample 1

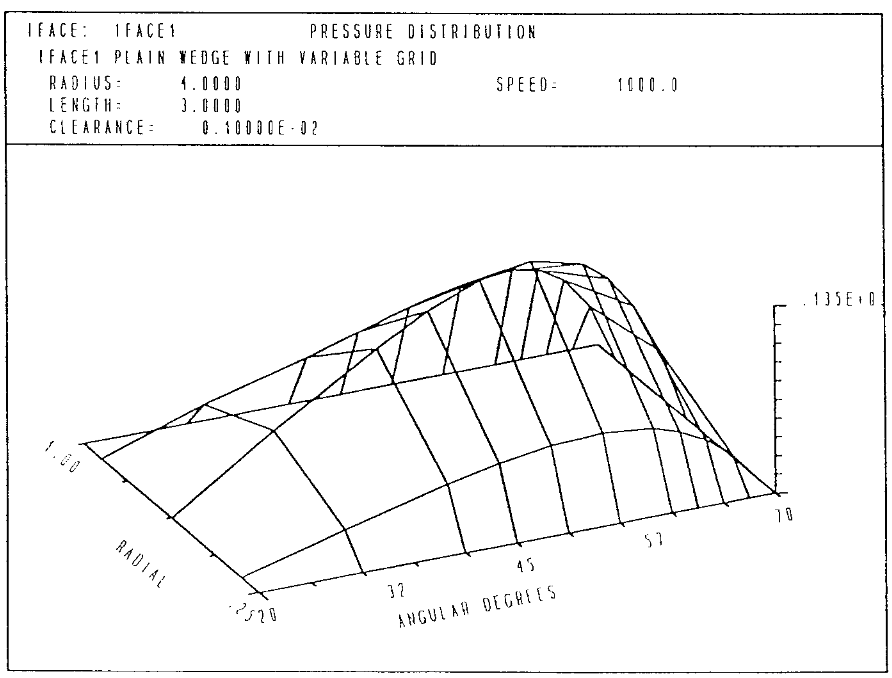

Figure 27. Pressure Distribution for Sample 1

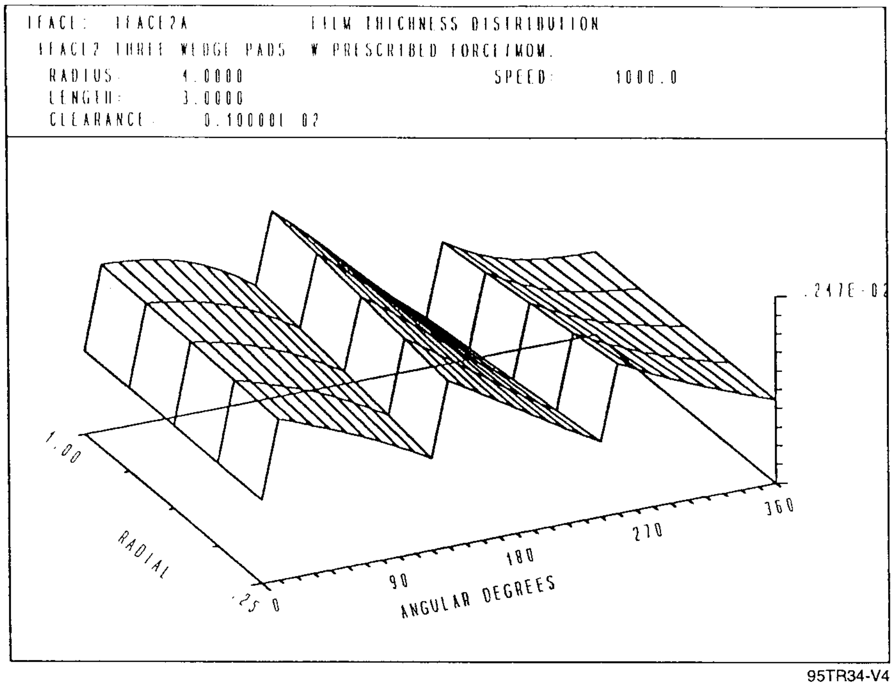

Figure 28. Film Thickness Distribution for Sample 2A

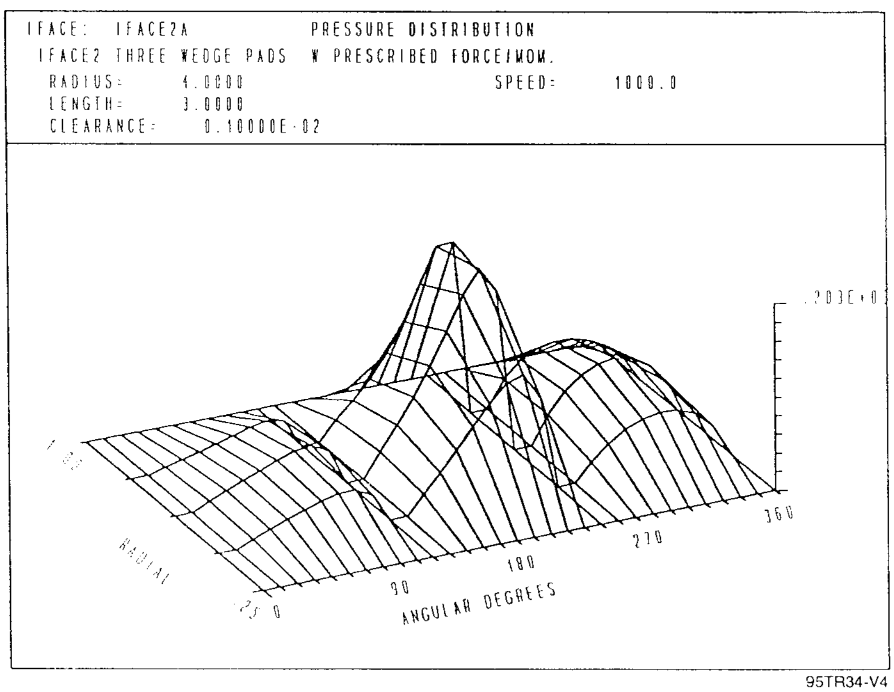

Figure 29. Pressure Distribution for Sample 2A

In sample **3B**, the fluid film forces are calculated for prescribed orifice diameters of 0.068 in., an axial eccentricity ratio* of 20% and a misalignment ratio of 50% about the y-axis (DORIF, EX, BETA). The pocket pressures converged in 4 iterations. The pressure increases in pockets 1 and 4 and decreases in 2 and 3. The fluid film axial force increases to 7,932 lbf, with resulting moments of -287 and -5,216 in.-lb about the x and y axes, respectively. The resulting film thickness and pressure distributions are shown in Figures 30 and 31, respectively.

In sample 3C, the external force and moment are prescribed equal to the negative of the fluid film forces calculated in sample 3B. The initial guess for pocket and film pressure distributions were read from the values saved previously in sample case 3A. Although convergence is also achieved in 4 outer loop iterations, it takes more time to execute (572 versus 360 seconds) because the program must now simultaneously iterate on three position variables as well as the four pocket pressures.

Sample 13 illustrates multiple inputs in the same run. The model consists of 4 preloaded pads, each with a preload ratio of 50% and a circumferential offset of 10°. The first input prescribes a roughness of 0.02 mils to both surfaces while the second and third inputs have smooth housing and rough rotor, and vice-versa. The last input restores smooth surfaces for both housing and rotor. The resulting film thickness is shown in Figure 32; the pressure distribution is shown in Figure 33. Table 3 illustrates the effects of surface roughness on the torque and direct stiffness coefficients. It is noted that roughness of the housing alone can increase the stiffnesses by 43 to 52% with less than 18% increase in torque, while roughness of the rotor alone decreases the stiffnesses with equivalent increase in torque.

Sample 17 illustrates a hydroynamically supported face seal. The sealed pressure at the inner radius is 1000 psi higher than the outer radius. Eight Rayleigh steps are equally spaced along the circumference and are fed from the inner radius by a deep radial groove. A misalignment ratio of 50% is specified about the x axis. The resulting film thickness is shown in Figure 34 and the pressure distribution is shown in Figure 35.

Samples 15A and 15B are similar to 3A and 3C, respectively, but with a finer mesh, which takes significantly longer execution times (2116 and 1702 sec). The resulting film thickness and pressure distributions are shown in Figure 36 and Figure 37.

*Prescribing EX=0.2 with CREF=0.001 is analogous to prescribing CREF=0.0012 with EX=0.0.

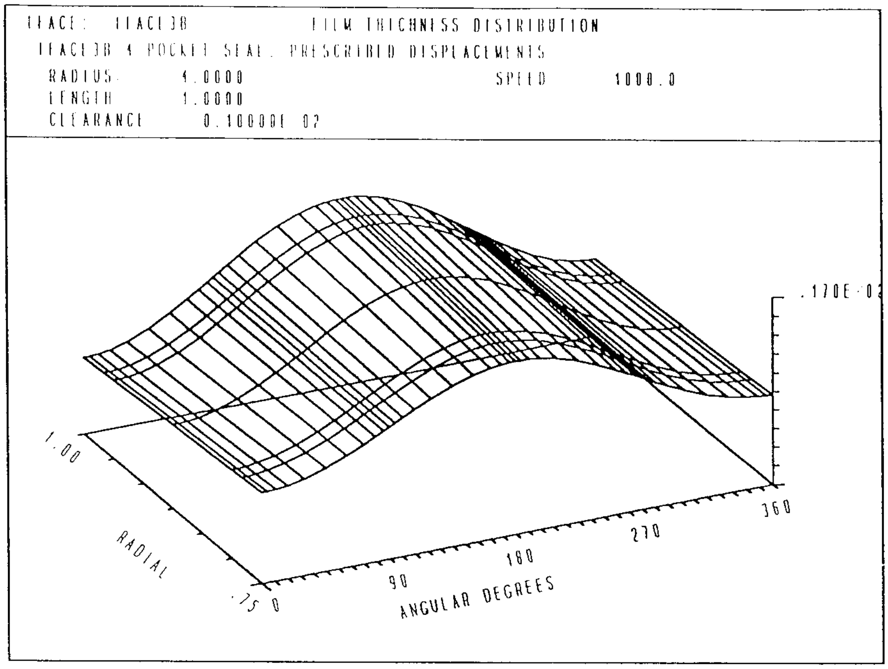

95TR34-V4

Figure 30. Film Thickness Distribution for Sample 3B

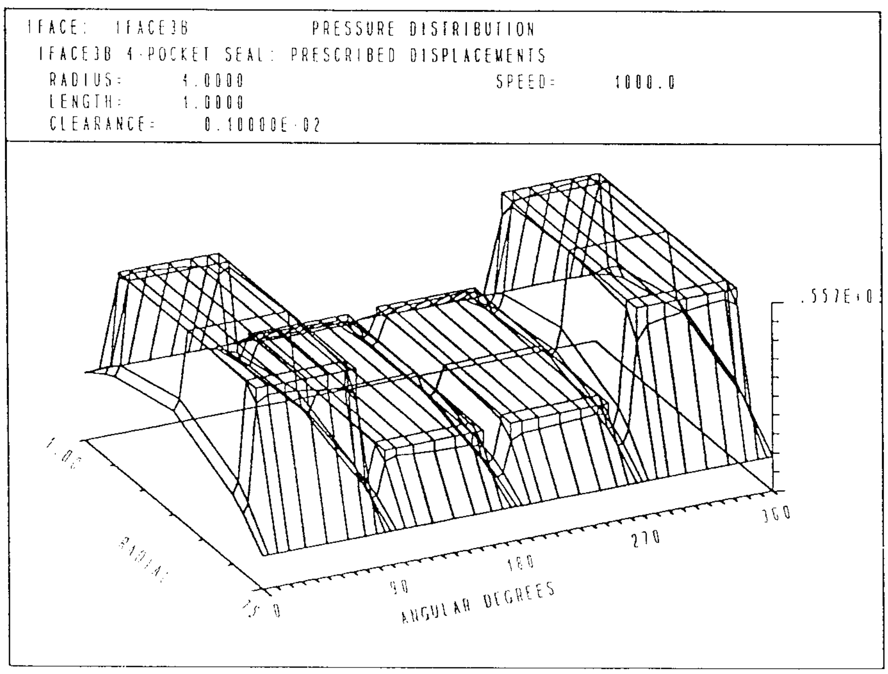

95TR34-V4

Figure 31. Pressure Distribution for Sample 3B

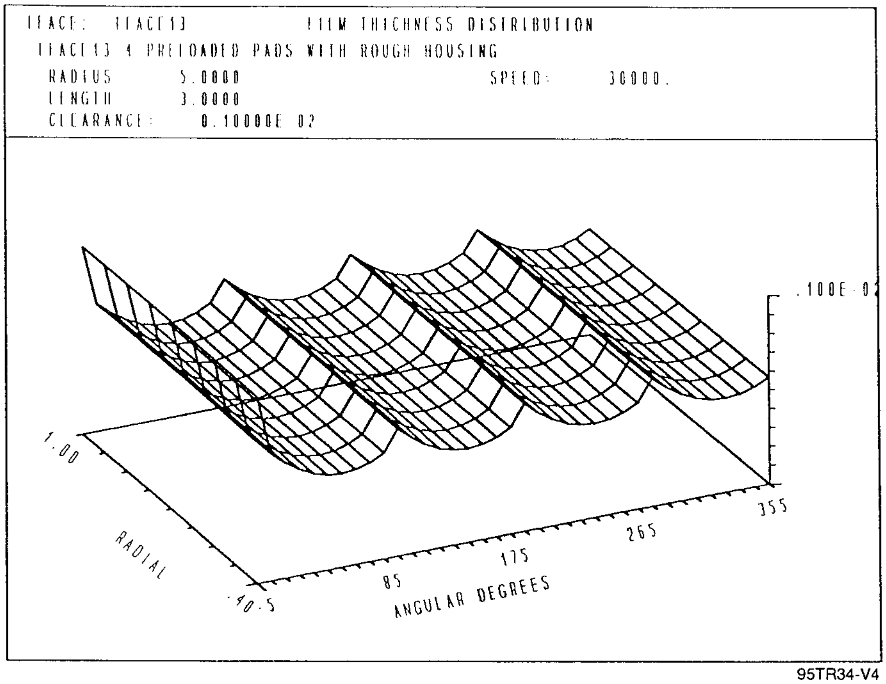

Figure 32. Film Thickness Distribution for Sample 13

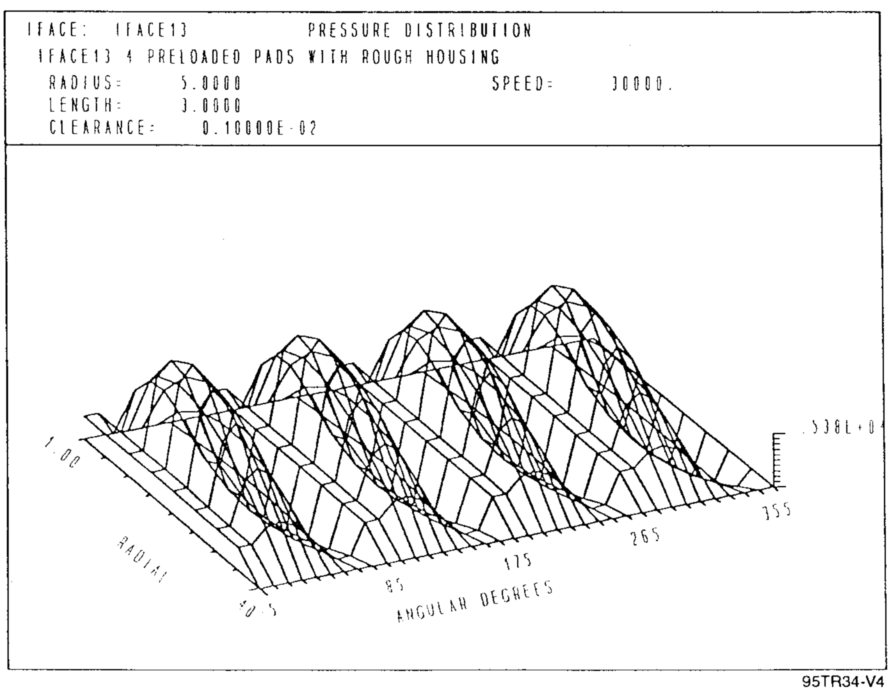

Figure 33. Pressure Distribution for Sample 13

Table 3. Effect of Roughness on Torque and Direct Stiffnesses

roughness (mils)		torque (in.-lb)	K_{zz} (10^8lb/in.)	$K_{\alpha\alpha}=K_{\beta\beta}$ (10^8lb-in./rad)
rotor	housing			
0.02	0.02	2,900	245	1,956
0.02	0.00	2,354	158	1,153
0.00	0.02	2,366	263	2,035
0.00	0.00	2,006	184	1,337

95TR34-V4

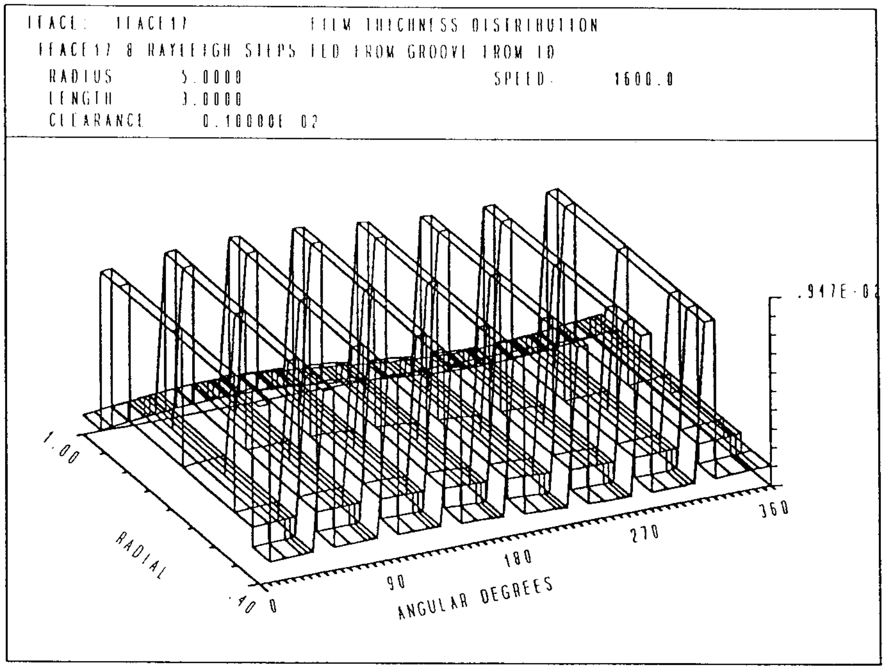

95TR34-V4

Figure 34. Film Thickness Distribution for Sample 17

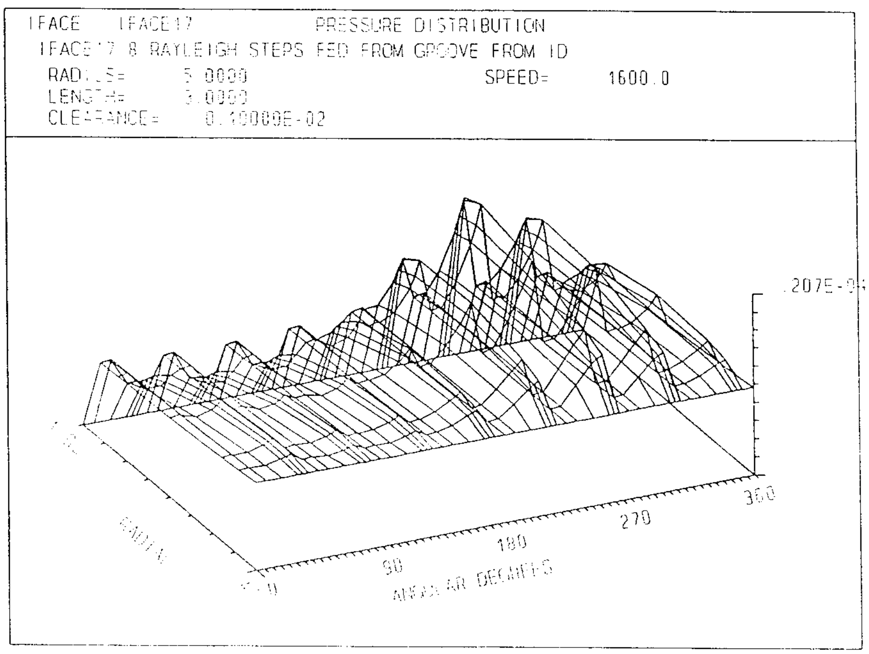

95TR34-V4

Figure 35. Pressure Distribution for Sample 17

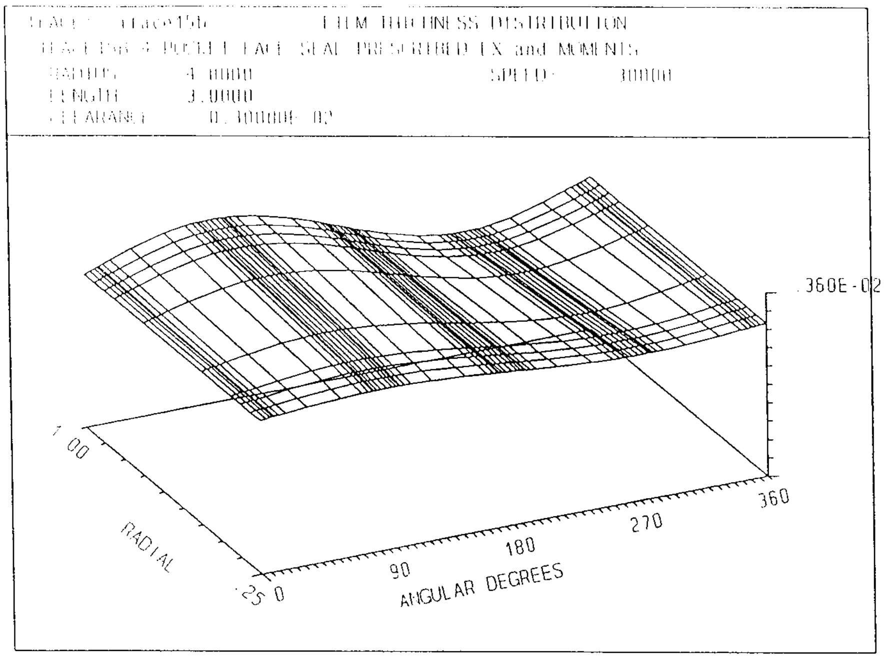

95TR34-V4

Figure 36. Film Thickness Distribution for Sample 15B

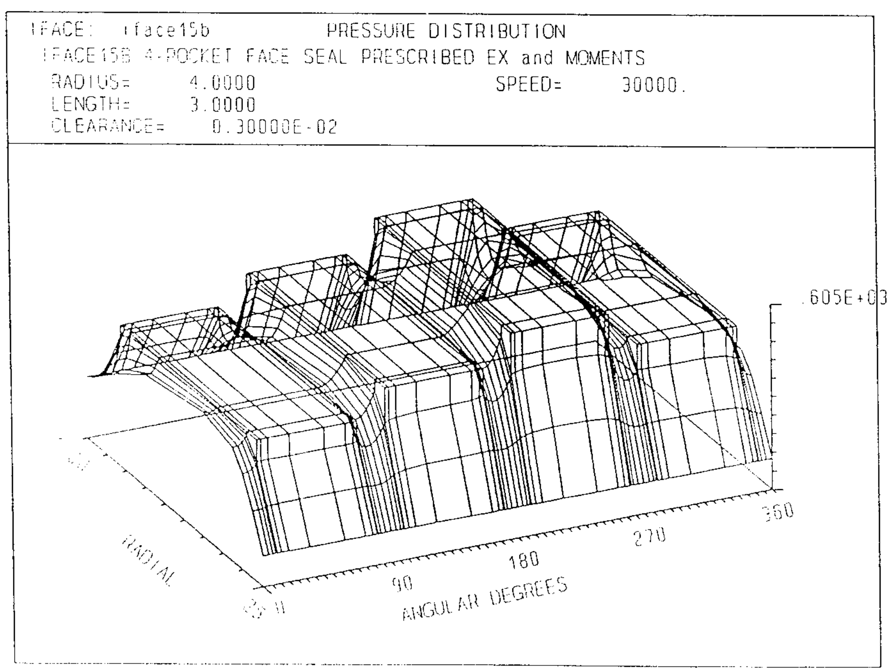

95TR34-V4

Figure 37. Pressure Distribution for Sample 15B

5.0 VERIFICATION

ICYL has been compared with the results of two other MTI computer codes as well as with currently published data. The first comparison was against a generic bearing program with many similar capabilities (GBEAR) based on the turbulent lubrication theory of Ng and Pan. A second comparison against a laminar bearing program (GASBEAR) was used to verify the calculations of moments and angular coefficients. Finally, comparisons were made against calculations published by San Andrés in Reference 14.

5.1 Comparison Against Other MTI Codes

The first of the MTI computer codes is GBEAR which is fully described in Reference 10. This program is based on the turbulent lubrication theory of Ng and Pan [13] and does not include surface roughness, housing rotation or calculation of misalignment coefficients. It includes inertia pressure drop at exit from pockets but not from seal ends.

Calculations were made with a 90° seal sector at an eccentricity ratio of 0.5 and with a pocket at its center with a prescribed pressure ratio of 0.5. Table 4 shows a comparison of pocket flow, orifice size, force, and stiffness and damping coefficients. As expected, comparisons of GBEAR against ICYL with the same friction model yielded nearly identical results. With the new friction model that includes surface roughness effects, ICYL calculates lower torque (-32%), lower pocket flow (-13%) and orifice size (-7%), and force components (-6%). Very good agreement in the stiffness coefficients (-4%), and slightly higher damping coefficients (+13%) are obtained.

Other comparisons against GBEAR in the laminar regime and without pockets yielded identical results.

A second MTI computer code with the fluid compressibility turned off (GASBEAR) was used to verify the calculation of the 24 stiffness and damping coefficients which involve rotor misalignment. GASBEAR was written for use in conjunction with plane journal bearings and cylindrical seals and does not treat turbulence or pressurized pockets. The comparison, in the laminar regime and with the same finite difference mesh, yielded identical coefficients.

5.2 Comparison Against Published Data

A detailed comparison was made of the five-pad hydrostatic bearing discussed by San Andrés in Reference 13. This high speed hybrid journal bearing operates at relatively high levels of pressurization and relatively low viscosity lubricants, in which the effects of pressure-induced turbulence become important. Fluid inertia may also be important. Figure 38 is a plot of the pressure distribution at the concentric position, while Figure 39 and Figure 40 plot it for 40% eccentricity ratio of the journal between pockets and over a pocket center, respectively. Reproductions of the corresponding pressure distributions published by San Andrés are included in the figures for comparison. It is noticed that the size of the pressure drops at the pocket exits (i.e., entrance to the film) as well as the general pressure distribution are comparable for both analyses.

Table 4. Comparison Against GBEAR

	GBEAR	ICYL IFRIC=0	ICYL IFRIC=3	ICYL IFRIC=4
Recess flow (in^3/s)	25.75	25.21	20.931	22.316
Orifice diam. (in)	0.0833	0.0820	0.0752	0.0776
Torque (lb-in)	14.38	14.32	8.791	9.771
Power (Lb-in/s)	45,171	44,971	27,617	30,696
Fx (Lb)	3,694	3,358	3,352	3,477
Fy (Lb)	-3,488	-3,122	-3,083	-3,346
Kxx (10^6 Lb/in)	2.352	2.267	2.329	2.344
Kxy (10^6 Lb/in)	-1.461	-1.378	-1.280	-1.397
Kyx (10^6 Lb/in)	-1.998	-1.874	-1.871	-1.961
Kyy (10^6 Lb/in)	1.573	1.481	1.406	1.564
Bxx (Lb/in)	232.08	234.79	269.01	274.46
Bxy (Lb/in)	-175.53	-175.87	-194.38	-199.65
Byx (Lb/in)	-174.78	-174.10	-192.40	-200.56
Byy (Lb/in)	173.87	173.79	187.57	196.53

95TR34-V4

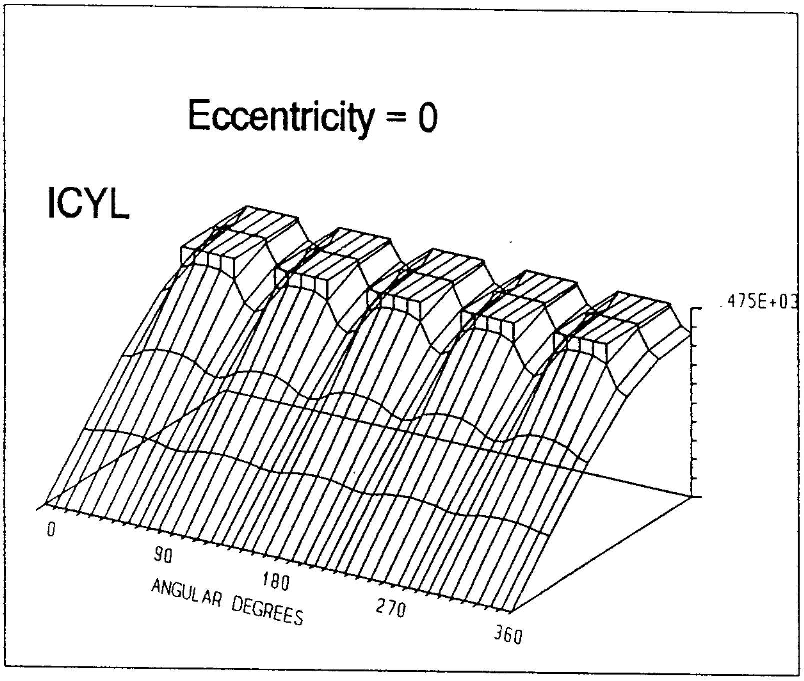

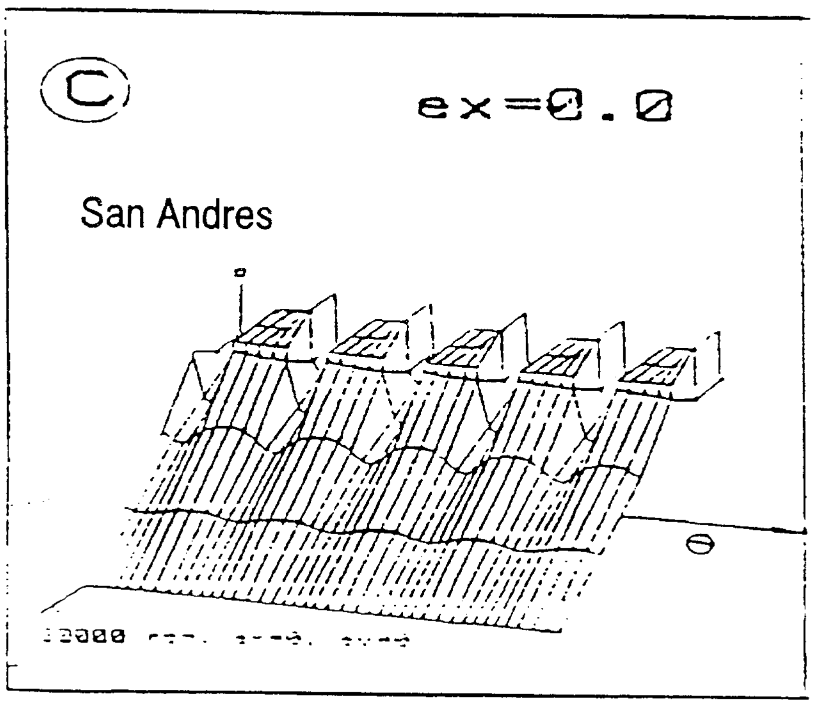

95TR34-V4

Figure 38. Comparison to San Andrés Five-Pad Bearing at Concentric Position

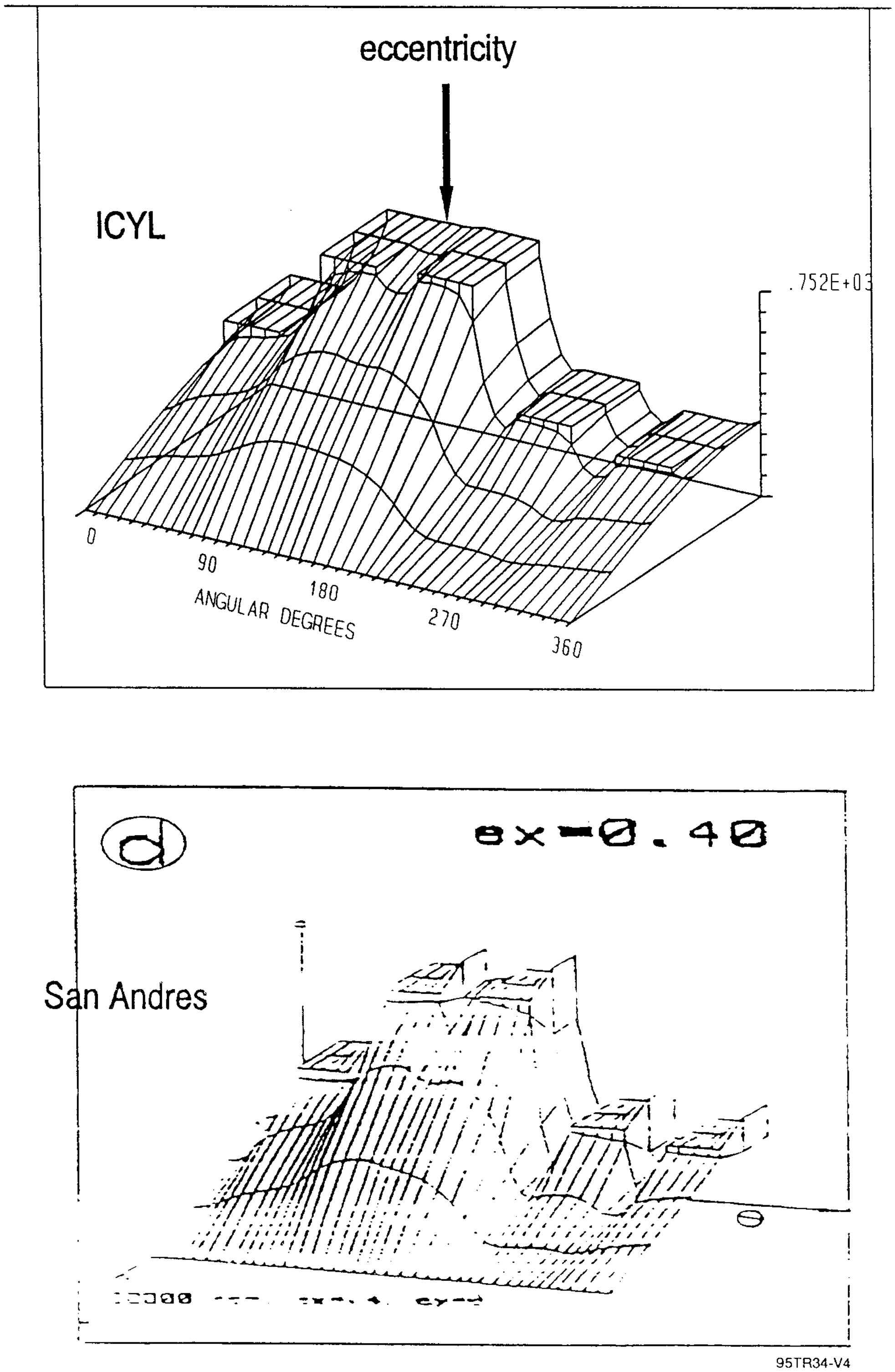

Figure 39. Comparison to San Andrés Five-Pad Bearing With 40% Eccentricity Between Pockets

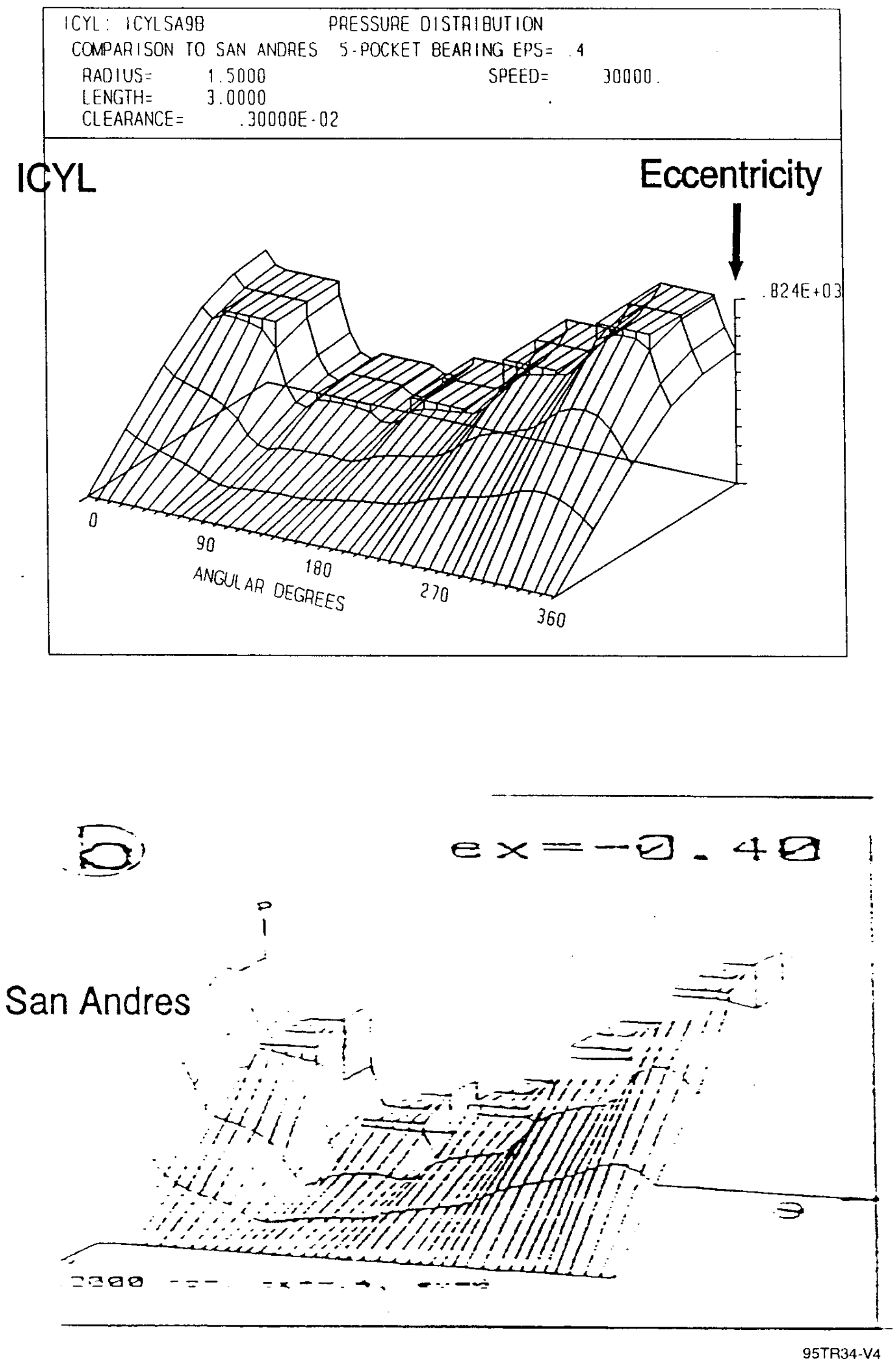

Figure 40. Comparison to San Andrés Five-Pad Bearing With 40% Eccentricity Over Pocket

At the concentric position, bearing flow requirements calculated by ICYL is 42 versus about 44ℓ/min reported by San Andrés. Figure 41 and Figure 42 are plots comparing the direct and cross-coupled stiffness coefficients and Figures 43 and 44 compare the direct and cross-coupled damping coefficients, respectively, versus eccentricity ratio. In general, ICYL predicts about 35% higher direct stiffness, 10% lower cross-coupled stiffness coefficients, and 15% lower direct damping at the concentric position. With increasing eccentricity ratio, the coefficients are observed to behave similarly and some of the discrepancies decrease. The cross-coupled damping coefficients with ICYL are equal in magnitude, opposite in sign and zero at the concentirc position, as is expected with an incompressible fluid. San Andrés non-zero concentric value (60 kN-s/m) is due to the fluid compressibility in the pocket. Figure 45 shows the critical mass versus eccentricity. The concentric value of 119 kg shows better stability than predicted by San Andrés, which predicts an unstable bearing with a 30 kg mass.

The analysis of San Andrés includes the effect of fluid inertia in the film as well as some special effects inside the pocket, such as fluid compressibility and a one-dimensional circumferential pressure rise downstream of the orifice. There is also a slight difference in friction law used: MTI's analysis follows the formula derived by Nelson [7] for the Moody diagram, in which the term containing the Reynolds number is raised to the 1/3 power while San Andrés uses the same formula with the power changed to 1/2.65 for a more restricted range of Reynolds numbers.

The above comparisons should provide reasonable verification, as the only discrepancies between the results can be explained by the different friction and inertia models between the codes.

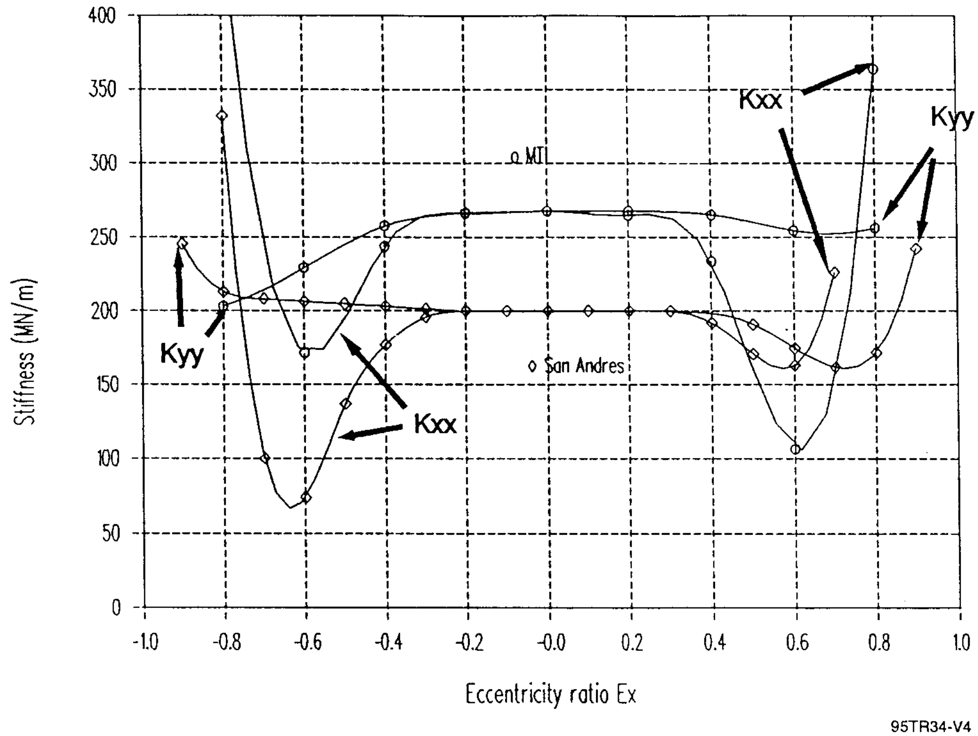

Figure 41. Comparison of Direct Stiffness Coefficient

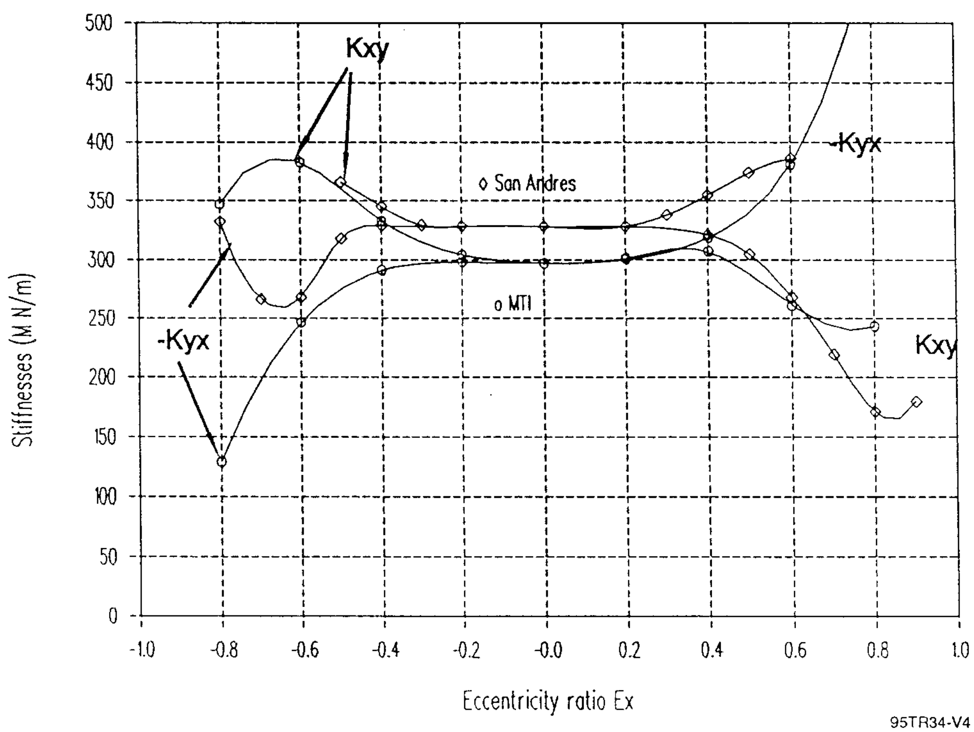

Figure 42. Comparison of Cross Stiffness Coefficients

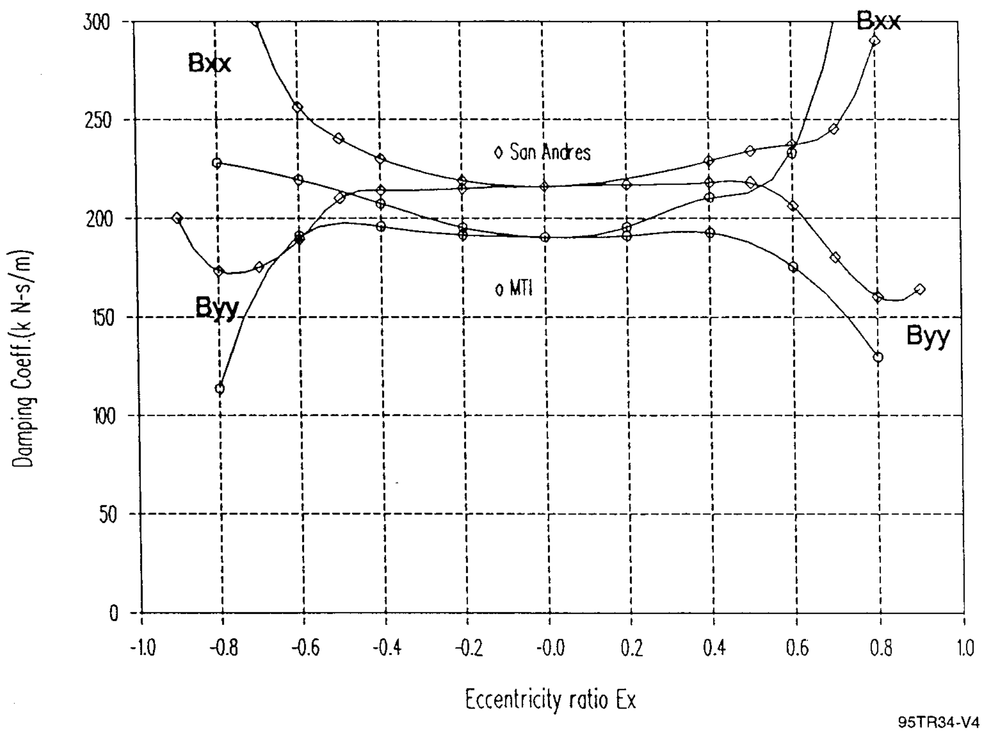

Figure 43. Comparison of Direct Damping Coefficients

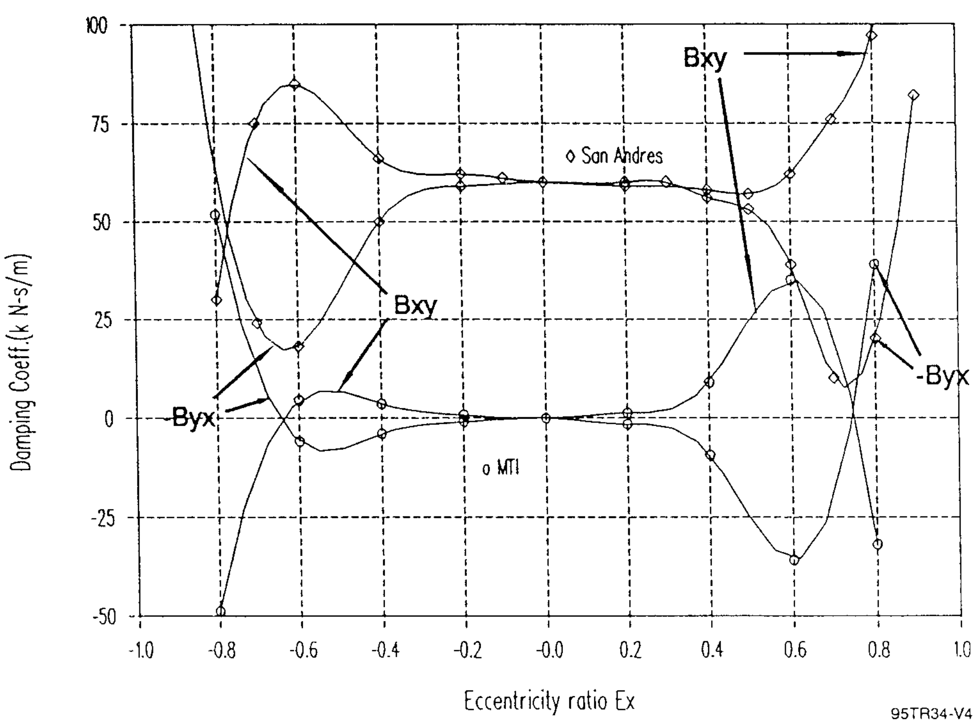

Figure 44. Comparison of Cross Damping Coefficients

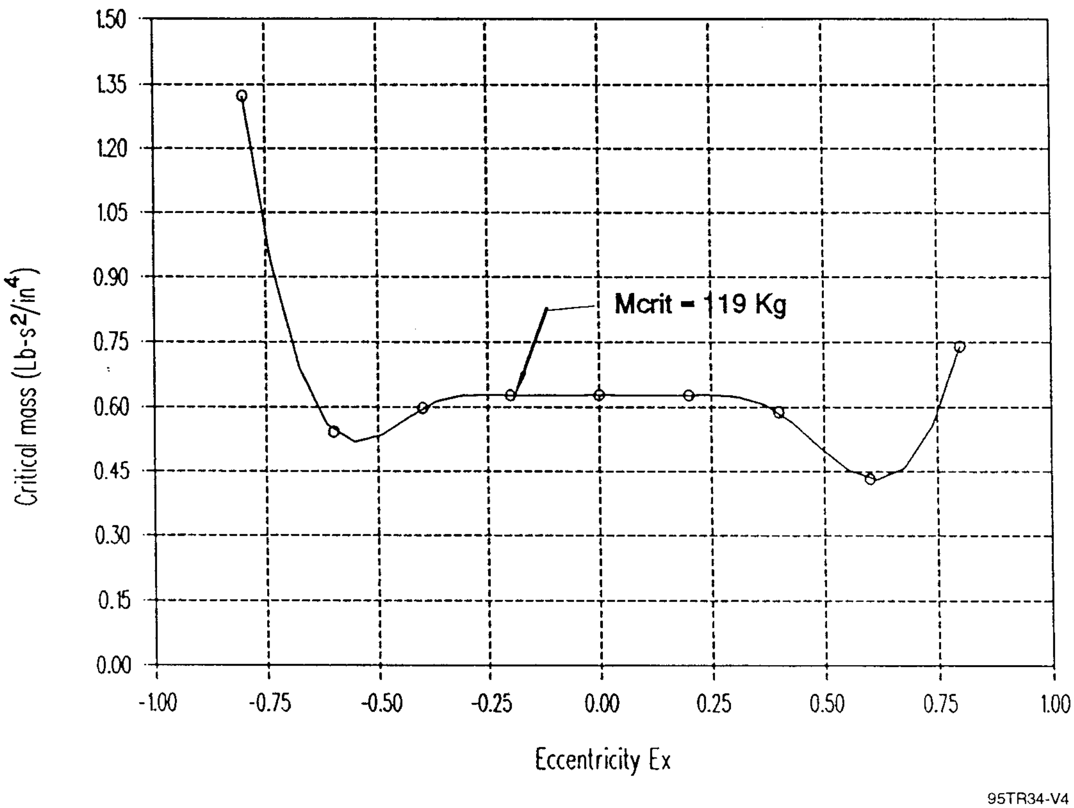

Figure 45. Critical Mass versus Eccentricity Ratio

6.0 REFERENCES

1. Munson, J., B. Steinetz, "Specific Fuel Consumption and Increased Thrust Performance Benefits Possible with Advanced Seal Technology," Preprint AIAA-94-2700 presented at 1994 Joint Propulsion Conference, Indianapolis, IN, June 27, 1994.
2. Artiles, A., *Users Manual for Computer Code ICYL, Cylindrical Seals Lubricated by Incompressible Fluids*, Mechanical Technology Incorporated, Technical Report 92TM13, November 1991.
3. Artiles, A., *Users Manual for Computer Code IFACE, Face and Cylindrical Seals Lubricated by Incompressible Fluids*, Mechanical Technology Incorporated, Technical Manual 93TM4, August 1993.
4. Launder, B.E., Leschziner, M., *Flow in Finite-Width Thrust Bearings Including Inertia Effects I — Laminar Flow,* Trans ASME, **Journal of Lubrication Technology**, pp. 330-338, July 1978.
5. Launder, B.E., Leschziner, M., *Flow in Finite-Width Thrust Bearings Including Inertia Effects II — Turbulent Flow*, Trans ASME, **Journal of Lubrication Technology**, pp. 339-345, July 1978.
6. San Andrés, Luis A., *Turbulent Hybrid Bearings with Fluid Inertia Effects, Part I: Analysis,* Submitted for publication at the ASME/ASLE Joint Tribology Conference, Toronto, Canada, October 1990.
7. Nelson, C.C., Ngyyen, D.T., *Comparison of Hir's Equation with Moody's Equation for Determining Rotordynamic Coefficients of Annular Pressure Seals*, Trans ASME, **Journal of Tribology**, pp. 144-148, January 1987.
8. Elrod, H.G., Ng, C.W., *A Theory for Turbulent Fluid Films and its Application to Bearings*, Trans ASME, **Journal of Lubrication Technology**, pp. 346-362, July 1967.
9. Castelli, V., Pirvics, J., *Review of Methods in Gas Bearing Film Analysis*, **Trans. ASME**, pp.777-792, 1968.
10. Artiles, A., Walowit, J., and Shapiro, W., *Analysis of Hybrid Fluid Film Journal Bearings with Turbulence and Inertia Effects*, **Advances in Computer Aided Bearing Design**, ASME Publication G00220, pp. 25-52, 1982.
11. Press, W.H., Flannery, B.P., Teukolsky, S.A. and Vetterling, W.T., *Numerical Recipes*, Cambridge University Press, 1986.
12. Castelli, V., *Design of Gas Bearings - Volume 1, Part 4: Numerical Methods*, **Gas Bearing Course Notes**, Mechanical Technology Incorporated, Latham, NY, 1971.
13. San Andrés, Luis, A., *Effect of Eccentricity on the Force Response of Hybrid Bearing*, submitted to STLE for publication, 1990.
14. Ng, Chung-Wah, Pan, C.H.T., *A Linearized Turbulent Lubrication Theory*, Trans ASME, **Journal of Basic Engineering**, pp. 675-688, September 1965.

REPORT DOCUMENTATION PAGE

Form Approved
OMB No. 0704-0188

1. AGENCY USE ONLY (*Leave blank*)

2. REPORT DATE
October 2004

3. REPORT TYPE AND DATES COVERED
Final Contractor Report

4. TITLE AND SUBTITLE
Numerical, Analytical, Experimental Study of Fluid Dynamic Forces in Seals
Volume 4—Description of Incompressible Fluid Seal Codes ICYL and IFACE

5. FUNDING NUMBERS
WBS–22–5000–0013
NAS3–25644

6. AUTHOR(S)
Antonio Artiles

7. PERFORMING ORGANIZATION NAME(S) AND ADDRESS(ES)
Mechanical Technology, Inc. (MTI)
968 Albany-Shaker Road
Latham, New York 12110

8. PERFORMING ORGANIZATION REPORT NUMBER
E–14708–4

9. SPONSORING/MONITORING AGENCY NAME(S) AND ADDRESS(ES)
National Aeronautics and Space Administration
Washington, DC 20546–0001

10. SPONSORING/MONITORING AGENCY REPORT NUMBER
NASA CR—2004-213199-VOL4

11. SUPPLEMENTARY NOTES
Project Manager, Anita D. Liang, Aeronautics Directorate, NASA Glenn Research Center, organization code 2200, 216–977–7439. Responsible person, Robert C. Hendricks, Research and Technology Directorate, NASA Glenn Research Center, organization code 5000, 216–977–7507.

12a. DISTRIBUTION/AVAILABILITY STATEMENT
Unclassified - Unlimited
Subject Categories: 07, 20, and 34 Distribution: Nonstandard
Available electronically at http://gltrs.grc.nasa.gov
This publication is available from the NASA Center for AeroSpace Information, 301–621–0390.

12b. DISTRIBUTION CODE

13. ABSTRACT ***(Maximum 200 words)***

The objectives of the program were to develop computational fluid dynamics (CFD) codes and simpler industrial codes for analyzing and designing advanced seals for air-breathing and space propulsion engines. The CFD code SCISEAL is capable of producing full three-dimensional flow field information for a variety of cylindrical configurations. An implicit multidomain capability allow the division of complex flow domains to allow optimum use of computational cells. SCISEAL also has the unique capability to produce cross-coupled stiffness and damping coefficients for rotordynamic computations. The industrial codes consist of a series of separate stand-alone modules designed for expeditious parametric analyses and optimization of a wide variety of cylindrical and face seals. Coupled through a Knowledge-Based System (KBS) that provides a user-friendly Graphical User Interface (GUI), the industrial codes are PC based using an OS/2 operating system. These codes were designed to treat film seals where a clearance exists between the rotating and stationary components. Leakage is inhibited by surface roughness, small but stiff clearance films, and viscous pumping devices. The codes have demonstrated to be a valuable resource for seal development of future air-breathing and space propulsion engines.

14. SUBJECT TERMS
CFD seal code; Industrial seal codes; User-friendly seal codes; Fluid-film seal codes; Clearance seal codes; Seals; Dynamics; Design; Computational analysis; Fluid forces

15. NUMBER OF PAGES
80

16. PRICE CODE

17. SECURITY CLASSIFICATION OF REPORT	18. SECURITY CLASSIFICATION OF THIS PAGE	19. SECURITY CLASSIFICATION OF ABSTRACT	20. LIMITATION OF ABSTRACT
Unclassified	Unclassified	Unclassified	